Master's Thesis

University of Applied Sciences Esslingen

Faculty of Mechanical Engineering

Project:

Feasibility Study of a UAV-Based Measurement System to Determine Heliostat Facet Surface Slope Errors

from

Robin Sättele

August 27, 2019

Supervisors:

Prof. Dr.-Ing. S. Rösler (University of Applied Sciences Esslingen)

Dr. M. Lubkoll (Stellenbosch University)

Eidesstaatliche Versicherung

Ich versichere hiermit, dass ich die vorliegende Arbeit selbstständig und nur unter Nutzung der angegebenen Literatur und Hilfsmittel angefertigt habe. Alle Stellen, die wörtlich oder sinngemäß aus Veröffentlichungen oder anderen Quellen entnommen sind, sind als solche eindeutig kenntlich gemacht. Die Arbeit ist in gleicher oder ähnlicher Form noch nicht veröffentlicht und noch keiner Prüfungsbehörde vorgelegt worden.

Stellenbosch, 27.08.19   R. Sel

Ort, Datum: Unterschrift

Geheimhaltung

Die vorliegende Arbeit ist als geheim eingestuft: Yes ☐   No ☒

Falls, ja so darf in die Arbeit nur für Prüfungszwecke Einblick gewährt werden. Weiterhin ist die Weitergabe des Inhaltes weder mündlich noch schriftlich an Dritte zulässig. Die Geheimhaltung gilt in der Regel 5 Jahre mit Beendigung der Arbeit.

Abstract

With the heliostat field being the largest cost driver of a CSP central receiver plant, its optical performance is essential for cost reduction. The optical performance of a solar field depends largely on the pointing accuracy and surface shape errors of the heliostats. Ageing, environmental influences and gravity change the shape of heliostat facets in-field in different angular positions. Suitable measurement solutions are required to assure the optical performance of the solar field. Unmanned Aerial Vehicles (UAV) provide high automation with aerial imagery by at the same time potentially low cost. This thesis summarizes a review of currently used measurement systems, their potential for an UAV-based system and an outlook on candidate technologies based on aerial imagery for heliostat surface characterization.

State of the art for industrial quality control of heliostat facets is typically carried out with deflectometry as the final step of production. Highly automated methods were already developed and deployed for parabolic trough concentrators with the furthest progress of an UAV-based measurement system. Heliostat in-field characterization tools still depend on a stationary set-up or the time-expensive photogrammetry method. Different solutions seem to be suitable for an UAV-based approach to characterize heliostat facets with a high automation and flexibility potential.

Kurzfassung

Das Heliostatenfeld is der größte Kostentreiber eines Zentralreceiverkraftwerks, ein hoher optischer Wirkungsgrad ist daher erforderlich um Kosten zu reduzieren. Der optische Wirkungsgrad des Solarfeldes hängt wesentlich von der Punktfokusgenauigkeit und Oberflächenfehlern der Heliostaten ab. Alterung, Umwelteinflüsse und Gravitation nehmen Einfluss auf die Form der Heliostatenspiegel im Betrieb in unterschiedlichen Lagen. Lösungen sind erforderlich, um einen hohen optischen Wirkungsgrad des Solarfeldes im Betrieb zu gewährleisten. Unmaned Aerial Vehicles (UAV), auch Drohnen genannt, bieten eine hohe Automatisierungsmöglichkeit bei gleichzeitig niedrigen Kosten. Diese Thesis gibt eine Zusammenfassung aktueller Messsysteme wieder und deren Potenzial für ein drohnenbasiertes Messsystem wird analysiert. Ein Ausblick für mögliche zukünftige Messsysteme, basierend auf Luftbildaufnahmen, zur Charakterisierung von Heliostatenoberflächen wird gegeben.

Nach dem Stand der Technik wird die Qualität der Heliostaten am Produktionsende durch Deflektometriemesssysteme gesichert. Hochautomatisierte Qualitätskontrollsysteme um Solarkonzentratoren zu vermessen sind bereits entwickelt. Diese sind allerdings meistens speziell auf Parabolrinnenspiegel ausgelegt. Die fortgeschrittenste Entwicklung stellt dabei ein drohnenbasiertes Messsystem, genannt QFly welches vom DLR entwickelt wurde, dar. Heliostaten können bisher nur eingeschränkt im Betrieb vermessen werden. Entweder sind dafür entwickelte Messsystem nur stationär anwendbar oder man ist auf die zeit- und arbeitsintensive Vermessung mittels Photogrammetrie angewiesen.
Verschiedene Lösungsmöglichkeiten sind denkbar um ein drohnenbasiertes Messsystem zur Vermessung von Heliostatenoberflächen, mit hohem Automatisierungsgrad und flexiblen Einsatzmöglichkeiten, zu entwickeln.

Acknowledgements

Contents

List of Figures

List of Tables

Nomenclature

Abbreviations

STERG   Solar Thermal Energy Research Group

UAV   Unmanned Aerical Vehicle

SCCAN   Solar Concentrator Characterization At Night

SSE   Surface Slope Error   mrad

RMS   Root Mean Square   mrad

CSP   Concentrating Solar Power

Symbols

C^i Continuouty till i-th derivative

$\vec{x}$ Spatial vector with length and direction

$\hat{x}$ Normalized vector

$\vec{a} \cdot \vec{b}$ Scalar product between a and b

$\vec{a} \times \vec{b}$ Cross product between a and b

u_e Pixel index of emitter

u_c Pixel index of camera

O' Optical center camera

$l(u_e)$ Light map which connects u_c with corresponding u_c

f Focal length

1 Introduction

1.1 Concentrating Solar Power (CSP)

All CSP technologies use a reflector system to concentrate the incoming solar power onto a receiver. A tracking system ensures that the sun is continuously focused on the receiver. The resulting heat is used to produce electrical power in a conventional steam generator. The high-temperature heat can also be used for industrial processes as process heat, water desalination, production of synthetic fuels or can be stored in thermal storages. The stored heat is used to drive a steam generator in times of less renewable energy production. This ability helps to increase the reliability of the electricity grid. A high proportion of future energy is provided by a mix of renewable energies.

Four main types of CSP technologies are developed: Parabolic trough collectors, central receiver systems, linear Fresnel systems and parabolic dish systems[Sol18]. The first technology used in an industrial application was the parabolic trough collector system. Today, around 90% of all operational CSP plants are parabolic trough system. However, since 2017 the fastest growing technology is the central tower system. This thesis will focus on these two main technologies: Central receiver system and parabolic trough.

A parabolic trough collector is straight in one dimension (y-direction) and curved as a parabola in x- and z-dimension what leads to a focal line of the reflector. The parabola is given by 1.1 with the focal length f:

$$z(x) = \frac{x^2}{4f}.$$ (1.1)

Parabolic trough systems use an absorber tube in the focal line to collect the solar power as seen in figure 1.1. The tracking system therefore only has to perform a

(a) Parabolic trough collector system (b) Central receiver system
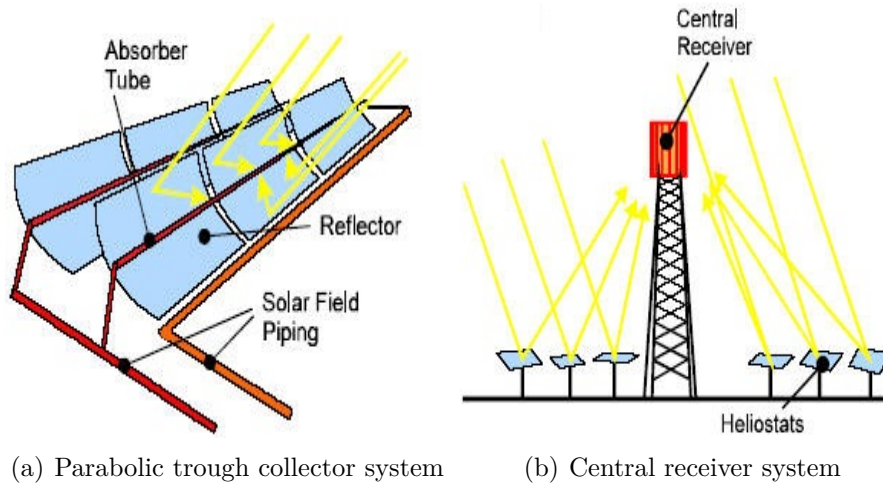
Figure 1.1: Most common CSP technologies (Images from [Sol18])

single-axis motion to ensure the focus of the sunlight falls onto the absorber tube. To protect the absorber tube from direct environmental influences it is enveloped by a glass tube. One concentrator assembly usually consists of many bent reflectors mounted on a frame to receive the parabolic shape. To obtain an overall focal line the reflectors require proper alignment and shape. The energy is absorbed by the central tube. A fluid flows constantly through the tube, usually a thermal oil, heats up from $293°C$ to $393°C$ and merges in the solar field piping. The collected energy, stored in the heated oil, is available for further usage. Cause of the small focus area of the concentrators only low-temperature applications are feasible.

Central tower systems use heliostats around the tower which concentrate the solar power onto one central receiver. A heliostat is by definition a reflective instrument to observe the sun and focus the reflecting sunlight towards a determined target. A small target area requires a focal point instead of a focal line which is illustrated in figure 1.1 b). A reflector has to be curved in all three dimensions, known as a paraboloid reflector. The elliptical paraboloid is received from 1.2 by adding the

second focal length in y-direction:

$$z(x) = \frac{x^2}{4f_x} + \frac{y^2}{4f_y}. \tag{1.2}$$

For large focal lengths in central receiver systems, the elliptical paraboloid can be approximated with a sphere. To focus the sun onto the receiver a two-axis motion is required for the heliostats with to independent focal lengths. Accessible temperatures, usually higher than $600°C$ and focus of all heliostats on one receiver, are much higher compared to the parabolic trough system. As a result, the target undergoes heating and cooling cycles cause of day and night as-well as environmental influences like clouds, which causes thermal stress. Therefore advanced materials are required. The generated heat at the receiver is transferred to a circulating molten salt. Salts have the characteristic of superior heat transfer and high heat capacities. Through complex field motion control, paraboloid shape manufacturing and higher accessible temperatures the development of a central receiver system which can operate for a long time required more time compared to parabolic trough systems. As industrial processes usually require high temperatures central receiver systems gained importance in the last years. Another benefit of the system is an increased energy-storage density derived by the higher temperatures compared to parabolic trough systems.

At the University Stellenbosch in South Africa the Solar Thermal Research Group (STERG) develops heliostats since 2011. In 2015 STERG introduced a Central Tower System called Helio100. Common systems use large heliostats with a central base set in concrete what makes the production and installation very expensive. Also, a failure of single heliostats due to environmental influences has a big impact on the entire solar field performance. As a result, these systems are only useful for large scale applications. In June 2015 the Helio100 project got popular through an article of *The Guardian* [Bar15] first time promising solar power to be cost-competitive to conventional sources in energy generation. Installation costs got radically reduced by development of a module called HelioPod (Figure 1.2).
One HelioPod consists of six heliostats with the dimension $1830m$ on $1220mm$. Each heliostat has a two-axis motion control performed by two linear actuators.
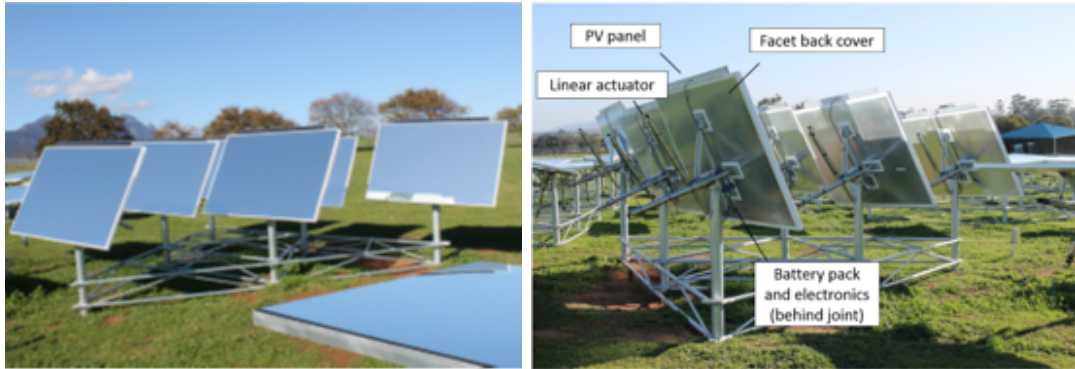
Figure 1.2: HelioPod

A photovoltaic panel connected to a battery ensures permanent availability of the heliostat. These heliostats are mounted on a frame build of tubes. Thus no expensive foundation of concrete is necessary and a fast set-up on any soil condition is given. After the heliostats are set-up on the field they calibrate themselves through an intelligent optical system and are ready to operate.

CSP technology is a high-performance application with a small receiver. For high efficiencies of gas turbines or particle receivers high constant temperatures and heat fluxes are required. The optical error function σ_{opt}, which gives a value for the focus quality of a heliostat can be expressed due to the combination of four individual error causes (1.3) after Lovegrove and Stein [LS12]:

$$\sigma_{opt}^2 = \sigma_{spec}^2 + \sigma_{surf}^2 + \sigma_{shape}^2 + \sigma_{canting}^2 \tag{1.3}$$

The specularity error σ_{spec} is caused by the scattering reflection which occurs on every material. After [LS12] the reflectivity[1] of a clean silvered glass mirror surface is around 0.93.

Small deviations from the optimum reflector shape lead to optical losses on account of receiver spillage. These errors are summarized in the surface slope error (SSE) σ_{surf}. Deviations occur on different scales. On a microscopic scale like surface roughness losses are negligible for glass reflectors. It is assumed the reflecting

---

[1]Reflectivity describes the ratio of reflected solar flux to incident solar flux
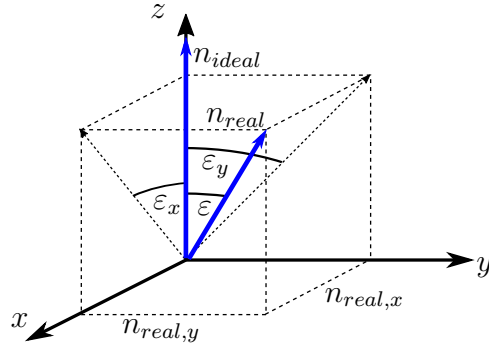
Figure 1.3: Surface Slope: Real and ideal surface slope normals

surface is perfectly continuous. Deviations on a small scale like local waves or bumps occur in the manufacturing process or through local stress. Facet shape deviations are not avoidable in the manufacturing process as bending a flat sheet of glass in two directions induces tensile stress in the material and leads to wrinkling also for large parabolic reflector radii. The Surface Slope Error ε (SSE) is the combination of these inaccuracies in one point of the reflector in $mrad$. The SSE can be divided into the two main directions ε_x and ε_y as seen in Figure 1.3.

On a large scale deviations result from wrong reflector orientations, insufficient canting or loads appearing on the structure during operation. They are included in the shape error σ_{shape}.

A real tracking system should focus the centre of the concentrated heat flux onto the centre of the receiver. Ideal tracking systems have uncertainties in motion control or offset values. This angular error can be characterized by the tracking error σ_{tr}.

The effect from the SSE on the solar power plant efficiency is analysed in a simulation with the ray-tracing software Tonatiuh[Bla11] . A varying SSE on the heliostats is applied to obtain the optical efficiency (η) of the solar system, the medium heat flux (Q_{in}) and the heat flux distribution with a maximum heat flux (q_{max}) on the receiver. The optical efficiency is defined as the ratio between energy reaching the receiver Q_{in} and the total energy from the solar source Q_{total}.

$$\eta = \frac{Q_{in}}{Q_{total}} \tag{1.4}$$
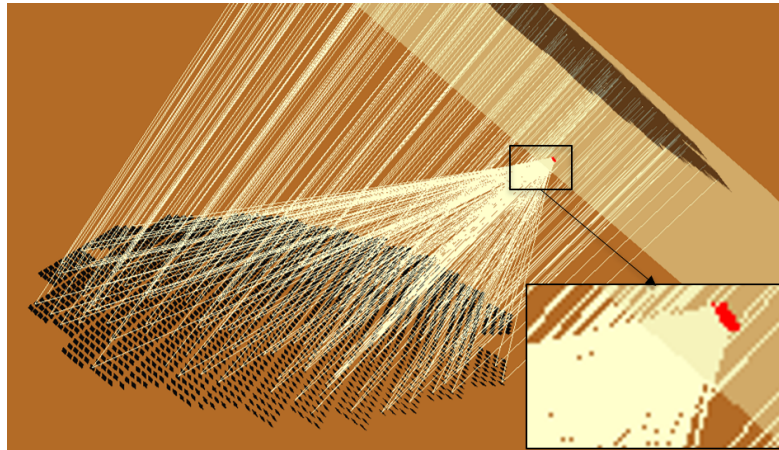
Figure 1.4: Tonatiuh model to analyse optical efficiency: The heliostat field is modelled with HelioPods and a total field size of $4956m^2$. The receiver disc has an aperture of $1m^2$. The sun is positioned at solar noon with an elevation of $60°$ and a Direct Normal Irradiance (DNI) of $1kW/m^2$.

Tonatiuh	SSE	0	0,5	1	1,5	2,5	3,5
Q_{in}	$[MW]$	4,456	4,282	3,898	3,385	2,334	1,573
q_{max}	$[MW/m^2]$	10,194	10,146	9,378	7,057	3,635	2,06
η		89,91%	86,4%	78,65%	68,3%	47,09%	31,74%

Table 1.1: Results from Tonatiuh ray-trace simulation: medium heat flux (Q_{in}), maximum heat flux (q_{max}) and optical efficiency (η)

The model in Tonatiuh is presented in Figure 1.4. Q_{total} is calculated from the product of the total solar field size and the DNI which leads in a Q_{total} of $4,956MW$. A varying SSE from $0mrad$ to $3,5mrad$ in steps is applied to analyse the optical efficiency of the system and the resulting heat flux on the receiver.

The results are shown in Table 1.1. Even with an SSE of $0mrad$ an optical efficiency of 100% cannot be reached. This is caused e.g. by losses through the reflectance of the concentrator, the transmittance of the glass cover or absorptance of the receiver. A maximum efficiency of $89,91\%$ is theoretically possible. With higher SSE then $1mrad$ the optical efficiency drops very fast and makes the system highly inefficient. The same result can be seen in the maximum heat flux. It stays on a stable level until the SSE exceeds $1mrad$. A stationary control system after the manufacturing process is state of the art to ensure the SSE does not exceed the threshold of $1mrad$. During operation in the field, the surface slope of the heliostat

can change due to gravitational load in different angular positions, mounting on a frame or environmental influences. Basic investigation studies show an average increase of the SSE of more than $1mrad$ from vertical to horizontal loose position [Mei14]. Following from this portable measurement systems are required to qualify heliostats in-field to ensure efficiency and durability of the solar field.

1.2 Research Purpose

As the optical efficiency of the solar thermal power plant is directly related to the efficiency of the solar field, measurement tools to qualify the state of solar concentrators are required. Small surface slope errors and deformations of the specular surface can occur over time during operation and lead to losses of optical performance. Yet, in-field measurement systems are rarely used for entire heliostat fields. Either high preparation effort is required before measurements are performed or dependencies on specific structures of the solar field make the measurement tool inflexible. In the last years, Unmanned Aerial Vehicles (UAVs) derived a high interest for industrial applications. Due to improved control and measuring systems UAVs provide a high level of automation and at the same time low costs. This thesis gives a contribution to the feasibility of a UAV-based automated in-field measurement tool to detect surface slope errors. A survey of currently developed measurement systems is investigated and possible solutions for the aerial approach are identified. The aim is a flexible, robust, fast and compact measurement tool for different CSP technologies under uncontrolled lighting conditions. The method has to be applicable for different solar concentrator shapes. For highest automation, a previous field preparation should be avoided. As UAVs are restricted to payload, a small and lightweight system is necessary.

2 Shape from Specular Reflection

Reconstruction of Lambertian objects is a well-known problem and many different solutions since 1991 [TD91] are successfully applied in industrial sectors. By contrast reconstruction of highly specular surfaces is still a widely open topic. This problem is caused by the characteristic of specular surfaces to reflect nearly every incoming light ray in one direction. As a result specular surfaces do not have their own appearance rather show the surrounding environment as seen in figure 2.1 b).

a) Lambertian reflector   b) Specular reflector
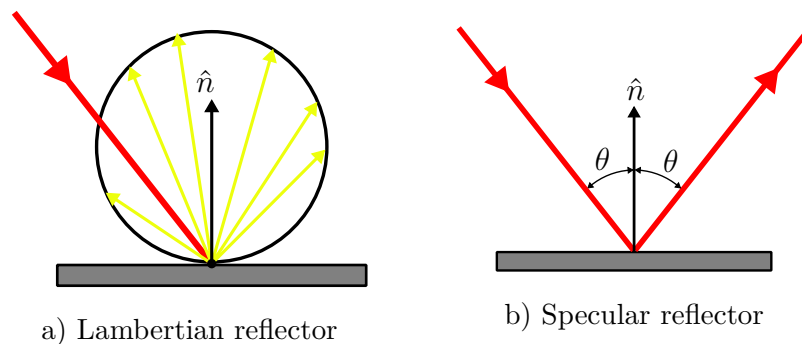
Figure 2.1: Lambertian and specular reflector

The fundamental approach of all optical measurement systems is the reflection of a light ray towards an optical detector via reflection on the specular surface. Computer graphics literature for ray tracers traditionally model the light ray reversed to the physical direction. The advantage is that only light rays are traced aiming the optical detector what leads in less calculation operations. This setup is presented in figure 2.2 and designed after Kammel [Kam05]. The ray emitter can be every defined light source or surface. Common for stationary systems is a setup with an image created by a screen or projector. The optical detector therefore can be a video or photo camera. We want to introduce the *simple light map l* as a
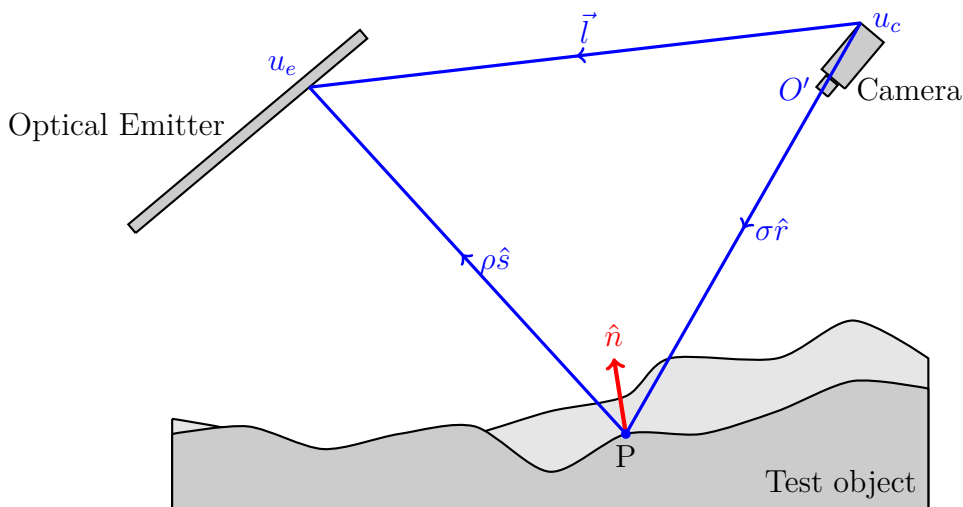
Figure 2.2: Fundamental optical measurement setup for specular surfaces

unique connection of corresponding Emitter pixel (u_e) and Observer/Camera pixel (u_c):

$$l : u_c \rightarrow u_e \tag{2.1}$$

The simple light map requires an emitter design which under any circumstances is uniquely defined. Processing of the captured images of the camera leads to the *simple light map*. Spatial coordinates of the system are not required for the *simple light map*.

If spatial coordinates of u_c, u_e and the point P on the test object are known the normal vector of the test object in P can be calculated with the two vectors $\vec{s} = \rho\hat{s}$ and $\vec{r} = \sigma\hat{r}$ in eq. 2.2:

$$\hat{n} = \frac{\vec{s} - \vec{r}}{\|\vec{s} - \vec{r}\|} = \frac{\rho\hat{s} - \sigma\hat{r}}{\|\rho\hat{s} - \sigma\hat{r}\|}. \tag{2.2}$$

Usually the straight forward option with known surface position P is not possible. The purpose of the measurement tool is to receive an unknown surface. Point P is part of this surface and thereby not accessible.

The light ray, starting from the camera sensor pixel u_c, intersects the test object in point $P = O' + \sigma\vec{r}$. A pinhole camera model is applied to the system and discussed in section (2.1.2). The parameter O' describes the optical centre of the pinhole

camera and defines the direction of $\hat{r}$ with the camera pixel u_c. The direction of the reflected ray is calculated via Snell's law (2.1.1) of reflectivity with the surface unit normal vector $\hat{n}$ in P:

$$\hat{s} = \hat{r} - 2(\hat{r} \cdot \hat{n})\hat{n} \tag{2.3}$$

The reflected light ray crosses the emitter plane in the point u_e:

$$u_e = P + \rho\hat{s} \tag{2.4}$$

With an absolute calibration of the camera and known spatial coordinates of u_c and u_e the *light map* $\vec{l}(u_e)$ is determined [1]. The calibration of the camera includes intrinsic and extrinsic parameters and is described in section 2.1.2. According to figure 3.3 the light map is calculated with eq. 2.7:

$$\vec{l}(u_e) = \sigma\hat{r} + \rho\hat{s} \tag{2.5}$$

$$\vec{l}(u_e) = \sigma\hat{r} + \rho(\hat{r} - 2(\hat{n} \cdot \hat{r})\hat{n}) \tag{2.6}$$

$$\vec{l}(u_e) = (\sigma + \rho)\hat{r} - 2\rho(\hat{n} \cdot \hat{r})\hat{n} \tag{2.7}$$

This leads in the two unknowns σ and ρ and therefore results in a one-dimensional solution space as seen in Figure 2.3. This is known as the *Inverse Problem.* For $\vec{l}(u_e)$ we can construct two rays $\hat{r}$ and $\hat{s}$ with σ and ρ which fulfils the coordinate requirements. But reflection point p and surface normal $\hat{n}$ change and result in ambiguous surface slopes. The light map can also be considered as a normal vector field in which the real solution space for each emitter to detector couple can be found. To solve the ambiguity additional data is required. Solutions for this problem are presented in section 2.2.

---

[1]The light map is also called *Geometric Mapping Function* or *Abbildungsfunktion* in German
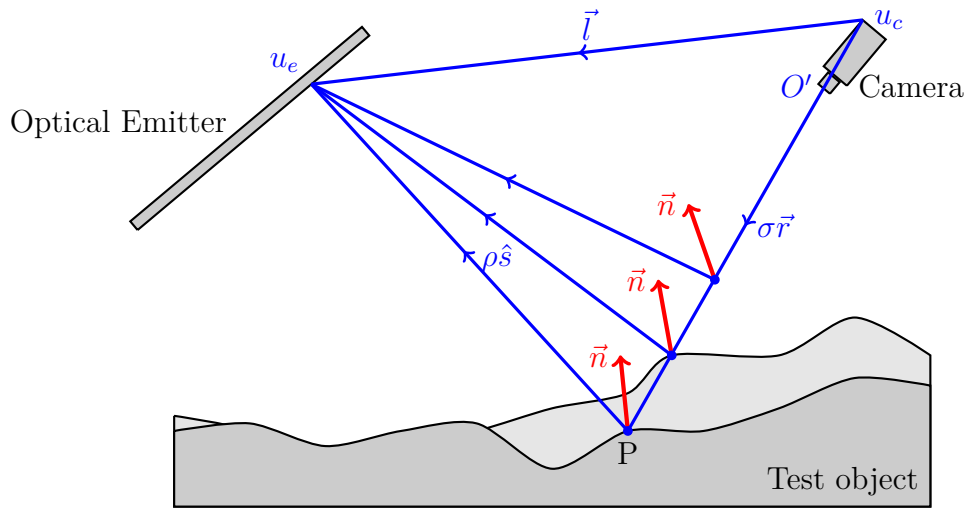
Figure 2.3: Inverse Problem

2.1 Background Theory

In this section basics are discussed for a better understanding of the following work. This includes the geometrical approach of a reflection, camera parameters plus internal ray modelling and a brief introduction of UAVs.

2.1.1 Specular Reflection

The heliostats reflect the incoming light rays from the sun. Therefore it is essential to know how the reflection in 3D space is calculated. A specular reflection at the mirror M is illustrated as 2D-graph in figure 2.4. This geometrical approach is also valid in 3D.
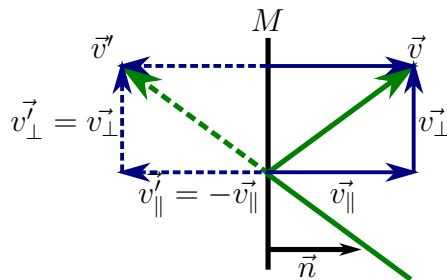
Figure 2.4: Specular reflection with geometrical approach

The initial ray $\hat{v}$ can be described in its perpendicular and parallel proportions:

$$\hat{v} = \vec{v_{\parallel}} + \vec{v_{\perp}} \tag{2.8}$$

Further the reflected ray $\hat{v}'$ depends on the proportions of $\hat{v}$:

$$\hat{v}' = \vec{v_{\parallel}'} + \vec{v_{\perp}'}$$
$$\hat{v}' = -\vec{v_{\parallel}} + \vec{v_{\perp}'} \tag{2.9}$$

The projection formula allows the calculation of the parallel proportion of $\vec{v_{\parallel}}$ depending on $\hat{v}$ and $\hat{n}$:

$$v_{\parallel} = (\hat{v} \cdot \hat{n})\hat{n} \tag{2.10}$$

The reflected ray $\hat{v}'$ is derived with the transformation from eq. (2.8) to $\vec{v_{\perp}}$ and the projection formula for $v_{\parallel}$:

$$\hat{v}' = \hat{v} - 2(\hat{v} \cdot \hat{n})\hat{n} \tag{2.11}$$

2.1.2 Camera Model

According to the illustration of the inverse problem a pinhole camera model is used for the optical detector. Only a single ray enters the aperture of the camera from any particular point of the scene. After Luhmann et al. [Luh06] the pinhole camera system is illustrated in figure 2.5. When the light rays pass the optical centre O' the real image is distorted by the lens system. As the optical centre O' and camera pixel coordinate u_c are used to calculate the direction of $\hat{r} = O' - u_c$ incorrect values are received. To compensate these distortions a camera calibration is required. For a better understanding of the following mathematical descriptions u_c' is described with its pixel positions x' and y':

$$u_c' = \begin{bmatrix} x' & y' \end{bmatrix}.$$

For the correction of appearing distortion effects the formulation of OpenCV[Bra00] is used. OpenCV is a powerful image processing package for the programming language *Python*. This software uses a structured pattern to calculate the magnitude
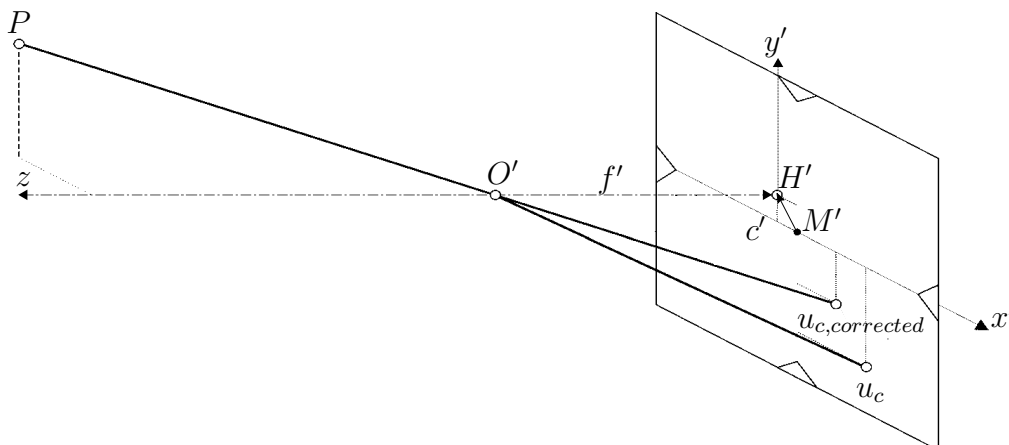
Figure 2.5: Interior camera orientation(Image adapted from [Luh06])
Usually the centre M' of the image is not on the optical axis. The principle point
H' is shifted from M' with the parameters c'_x and c'_y. The distance from the image
plane to the optical centre is only described by the focal length f'.

of the distortions and gives a mathematical model to reverse them. A checkerboard
with known side-lengths is used to calibrate the intrinsic and extrinsic parameters
from different orientations. The extrinsic parameters describe the camera's position
and rotation in real-world coordinates while the intrinsic parameters describe the
path a ray takes in the optical system of the camera. Two major distortions affect
the images received on the sensor: radial and tangential distortion. Both depend
on the image radius r' which is described as the distance from u_c to the principal
point H'

$$r' = \sqrt{x'^2 + y'^2} \tag{2.12}$$

Real lines appear curved on the image. This effect is based on the radial distortion
and magnifies with increasing distance to the optical centre of the image. Radial
distortion is eliminated with a polynomial series for each direction:

$$x'_{corrected} = x'(1 + k_1 r^2 + k_2 r^4 + k_3 r^6)$$
$$y'_{corrected} = y'(1 + k_1 r^2 + k_2 r^4 + k_3 r^6)$$

Tangential distortion occurs because the camera lens is not perfectly parallel aligned
to the imaging plane. Some areas in the image look closer then expected. The

tangential distortion is eliminated with the following equations:

$$x'_{corrected} = x' + \left(2p_1 x' y' + p_2(r'^2 + 2x'^2)\right)$$
$$x'_{corrected} = y' + \left(p_1(r'^2 + 2y'^2) + 2p_2 x' y'\right)$$

Further required informations are the intrinsic parameters: focal lengths (f'_x, f'_y) and the optical centres (c'_x, c'_y). These parameters can be summarised to the camera matrix:

$$\text{camera matrix} = \begin{bmatrix} f'_x & 0 & c'_x \\ 0 & f'_y & c'_y \\ 0 & 0 & 1 \end{bmatrix}$$

These parameters are calculated by taking and analysing a series of images from a well defined pattern like a chessboard. Corners on the pattern are detected. With knowledge of the distance between corners in real world coordinates the image relations are calculated and distortions eliminated. A ray tracing from each image sensor point u_c to O' is available and thereby $\hat{r}$.

As the test objects surface is specular it gets a part of the optical system, two focus settings for the camera are possible: Focus on the test object or the emitter pattern (Fig 2.6). If the camera is focused onto the test object, a high lateral resolution is obtained on cost of blurred screen images. This causes low angular resolution. On the other hand with the camera focused onto the screen the opposite is achieved. A compromise between lateral and angular resolution according to the system conditions is unavoidable.

2.1.3 Unmaned Aerial Vehicle (UAV)

A wide variety of UAVs, commonly known as drones, are available for hobbyists, military or commercial purposes. This leads to different specifications in price ranges and abilities. The military is interested in long-range surveillance drones which are mostly controlled by a computer system. Contrary hobbyists control the UAVs via controller for races or aerial imagery with camera and gimbal for added image stability. Through the full control from ground stations of UAVs, by

a) Focus on screen with high screen image resolution

b) Focus on test object with high lateral resolution
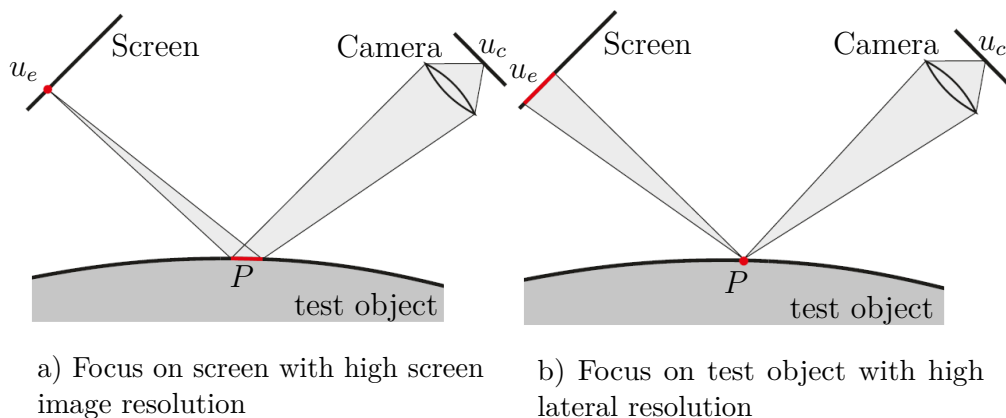
Figure 2.6: Possible focus settings for the camera (Images adapted from [BLF12])

at the same time low installation costs, they are used for commercial applications with their ability to carry additional weight and the performance of aerial imagery. Implemented for the survey of crops, inspection of infrastructure like oil pipelines or power lines, UAVs give a contribution to various industrial sectors[RGM16]. UAVs appear in different variations. While industry mostly uses a quadcopter with four parallel rotors, also tricopters, hexacopters and octocopters are available. Two quantifiable accuracies have to be considered when a UAV performs measurement experiments: Control and measurement accuracy.

Control accuracy describes the response of a UAV to a movement command. Four actuators are used to control the position of a quadcopter. Two opposite located actuators describe an actuator pair. Thereby one pair turns clockwise and the other anti-clockwise to avoid spin. A general control system for quadcopters is described by Gheorghiţă et al. [Ghe15]. When one pair increases thrust the UAV starts to rotate without translational motion. For moving up all actuators increase thrust, on the opposite for going down they decrease. To change direction a pair of actuators operates with different thrust.

Of higher interest for an optical measurement tool is the current position of the UAV which is referred to the measurement accuracy. The GPS-system is used to estimate a UAVs position. Common GPS systems achieve localisation accuracies around $3m$. An advanced set-up for commercial applications is the *Differential Global Positioning Systems* (DGPS) with real-time kinematic (RTK-GPS). This system provides accuracies on centimetre-level relative to the calibrated stationary

base [Nor08]. This is sufficient to perform a flight according to a specified path. For a measurement tool which calculates surface slope errors far below $1mrad$ this might be insufficient. Furthermore, the relative positions of the heliostat and detector are required. It is unlikely that heliostat positions are accessible on centimetre-level according to the stationary base of the RTK-GPS. A possible solution of this problem is discussed in section 3.2.

2.2 Regularization of the Inverse Problem

The previously introduced ambiguity of eq. (2.7) requires additional data to solve the inverse problem and reconstruct the specular surface. Computer science literature calls this step regularization of the inverse problem. Therefore the data acquisition is completed and the light map $l(u_e)$ is accessible for every camera pixel u_c. For the regularization, it is assumed that the specular surface is sufficiently smooth to be at least C^2-continuous. This means that local surface curvature is constant and has a unique normal vector. This assumption seems to fit very well for specular surfaces. After the inverse problem is solved a point cloud with correlated normal gradient field is available for the reconstruction in section 2.3. A brief summary of different regularization methods is given by Balzer and Werling [BW10]. At first, a short review of the methods polarisation and approximation is given. Afterwards, the two most promising and used regularization methods stereo view and triangulation are presented. Shape-from-shading is not considered in this work as it is purely based on shading information of diffuse reflections.

During a reflection of light, the previously unpolarized light is polarized depending on the reflection angle and reflective material. With the degree of polarisation, the direction of emitter pixels $\hat{s}$ can be reconstructed. Polarisation was first introduced by Rahmann and Canterakis [RC01] to characterize the shape of specular surfaces. with a rotating polarization filter in front of the camera and a series of pictures to receive sufficient data points, it is possible to reconstruct the surface. The degree of polarization depends strongly on the reflective material. Many data sets are required for an accurate determination of the reflection.

If the surface model of the test object is well-known, this knowledge can be used to estimate missing model parameters. Tarini et al. [Tar05] approximated an initial
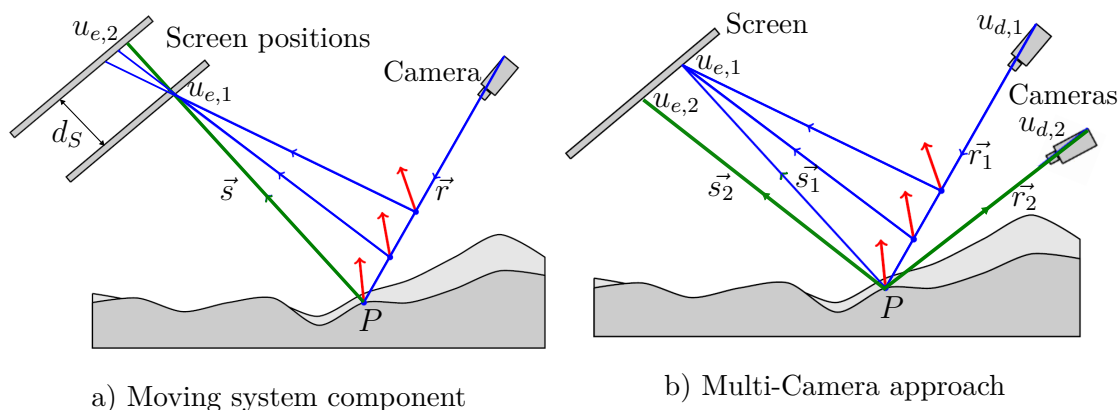
Figure 2.7: Stereo regularization approach

depth value to a random point. The depth map is calculated and with respect to the assumed surface model the initial value is optimized with the new values. The success of this method depends highly on the chosen initial value. If the initial value is far away from the real value the method may converge to a local minimum which maps a wrong surface.

2.2.1 Stereo View

The stereo view can be considered as the traditional regularization approach. By measuring the same object point from different viewing points the object distance can be calculated according to the observer. This can be obtained from two different measurement set-ups. If the screen is moved between two measurements different normal fields are received as illustrated in figure 2.7 a)[Rap12]. The previously unknown direction of $\hat{s}$ is calculated with the spatial positions of $u_{e,1}$ and $u_{u,2}$ and the known moving distance d_S. This leads to an explicit solution for the reflection point P. Required are only the real-world coordinates of the screen and the camera while the information of the object depth is obtained from the images. The second variation of the set-up is a multi-view camera approach with at least two calibrated cameras [KKH04] or a single moving camera. A possible set-up is illustrated in figure 2.7 b). Two different normal fields $\hat{n}_1$ and $\hat{n}_2$ are received for each camera. Spatial points can be considered as possible surface points when the

normal directions of the two normal fields are similar. This can be expressed by a simple disparity measure, in which the discrepancy between $\hat{n}_{1,P}$ and $\hat{n}_{2,P}$ attains its minima:

$$d(x,y,z) = \left\| \hat{n}_1^2(x,y,z) - \hat{n}_2^2(x,y,z) \right\| \tag{2.13}$$

The Stereo view approach can be used for the estimation of initial values but also the reconstruction of entire specular surfaces. With the assumption of a continuous surface, a searching algorithm can be applied and find neighbouring surface points for the entire object. Using multiple cameras with overlapping viewing areas provides a compact measurement set-up with high accuracy is achieved. The common deflectometry systems in section 3.3 use this approach for the end of production line quality control.

2.2.2 Region Growing Approach

In case only several points of the test object are known the surface can be reconstructed with the region growing approach. The method doesn't require a specific acquisition of data points what makes it applicable in various situations. Many cases show that a laser triangulation gives accurate initial values for the region growing approach, but also the previously discussed stereo view derives sufficient data points. The following region growing algorithm is well discussed by Scott and Burgess [SB10], Kammel [Kam05] and Horbach [Hor07].

The local curvature is assumed to be zero, only small surface changes occur between two measuring points. This condition is approximately satisfied for small increments. Then the surface can be modelled as a flat surface increment in figure 2.8. Extrapolating perpendicular to $\hat{n}_1$ till the intersection with $\sigma_2 \hat{r}_2$ is reached leads to the approximation of object point P_2. The new surface normal direction $\vec{n_2}$ is approximated and an iterative process is started over the entire surface. This approach is accurate dependent on the initial value as deviations grow with increasing distance to the starting point.
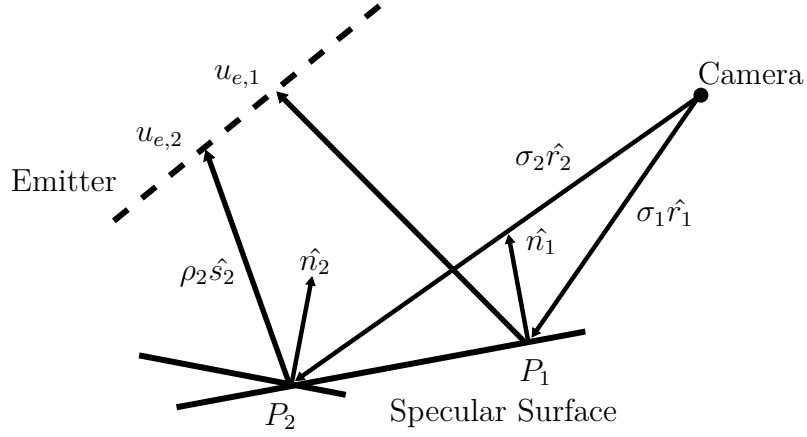
Figure 2.8: Region Growing Approach

The surface increment S is described with the Hesse normal form of a plane:

$$(\sigma_2 \hat{r}_2 - \sigma_1 \hat{r}_1)\hat{n}_1 = 0 \tag{2.14}$$

This leads to the distance value σ_2 of the intersection $P_2 = \sigma_2 \hat{r}_2$ with the plane S:

$$\sigma_2 = \sigma_1 \frac{\hat{r}_1 \hat{n}_1}{\hat{r}_2 \hat{n}_1} \tag{2.15}$$

With the spatial position of P_2 and the direction of $\hat{s}$ towards the emitter point $u_{e,2}$ the spatial position of $u_{e,2}$ is determined and thereby n_2:

$$\hat{s}_2 = u_{e,2} - \sigma_1 \frac{\hat{r}_1 \hat{n}_1}{\hat{r}_2 \hat{n}_1} \hat{r}_2 \tag{2.16}$$

With $\hat{s}_2$ and $\hat{r}_2$ the new surface normal unit vector $\hat{n}_2$ is received:

$$\hat{n}_2 = \frac{\hat{s}_2 - \hat{r}_2}{\|\hat{s}_2 - \hat{r}_2\|} \tag{2.17}$$

As mentioned iterative methods tend to accumulate calculation errors with increasing distance to the initial value. This drift cannot be avoided, even with more sophisticated numerical integration methods like Runge-Kutta. As a result, the

region reconstructed by one initial value should be limited. This is achieved by considering multiple initial values. The basic approach remains unchanged. For each initial value an entire surface mapping is carried out. Retrieved object points close to the initial point show higher accuracy than the points further away. This is considered for each surface reconstruction in weighting factors according to the distance of the initial value for each reconstructed object point.

2.3 Surface Reconstruction from Gradient Data

After the regularization a meshed point cloud with correlated normal gradient field is available. To obtain the SSE from figure 1.3 the reference surface is required to calculate $\hat{n}_{ideal}$. As the data is collected to obtain the surface properties it is not recommended to use the desired surface as a reference. As a consequence indicated measurement errors, caused by the unknown shape of the concentrator, would appear. To avoid those measurement errors the SSE is minimized by fitting a second-order polynomial to the point cloud. A general polynomial is given in eq. 2.18 by a quadratic surface:

$$z(x,y) = Ax^2 + By^2 + Cx + Dy + Exy + F \tag{2.18}$$

With perfect input data, three points are sufficient to get the ideal surface slope. Due to noise, measurement errors and numerical drift, the input of all data points are required for a least-square method. Real measurements produce outliers which have to be excluded before optimizing the surface[Kam05]. This is achieved e.g. with the implementation of a maximum deviation from the ideal surface slope. The reconstruction gets even more complex with the location-dependency of the normal gradient field. It depends on the distance σ to the camera and the light map $\vec{l}(u_e)$ what means with each iteration step of the least-square method the normal gradient field has to be recalculated. A short procedure of the iterative least-square method is given below:

With an initial guess, the first ideal surface is calculated. The intersection points of the camera pixel u_c have to be recalculated with the new ideal surface. With these surface points the ideal $\hat{n}_{ideal}$ and measured $\hat{n}_{real}$ surface slopes are calculated.
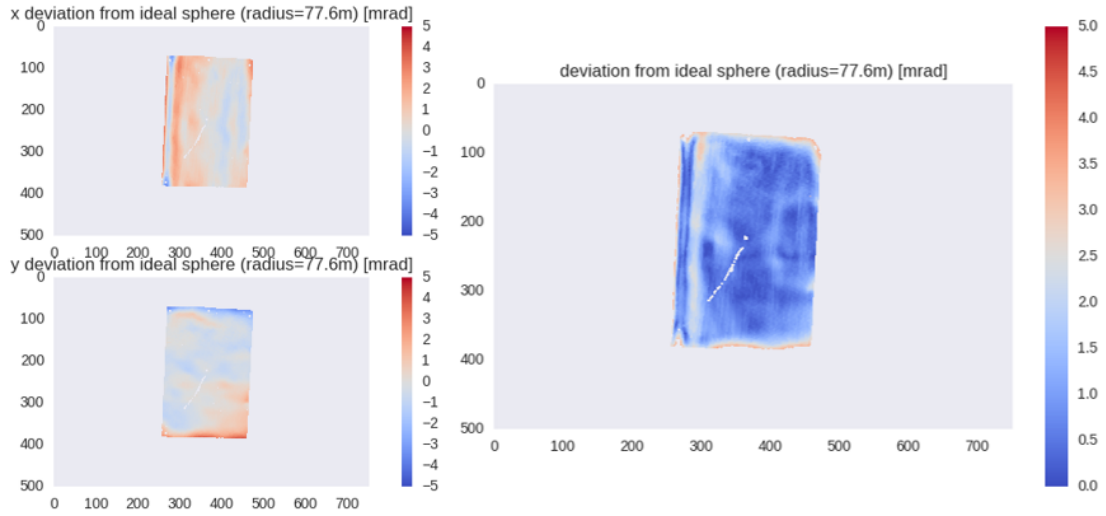
Figure 2.9: Result of measuring the SSE of a concentrator with the ZEBRA system On the left side, the deviations in x- and y-direction are illustrated. The SSE increases in direction to the edges. On the right side, the spatial deviations are visible. Outliers with a deviation higher then $5 mrad$ are excluded from the optimization algorithm.

By using the least-squares method a new quadratic surface is determined. The optimized values are the measured surface points. This procedure repeats until the abort criterion of eq. 2.19 is exceeded:

$$error = new\_surface\_coefficients - previous\_surface\_coefficients \tag{2.19}$$

This abort criterion is defined by the coefficients of the quadratic surface. When changes are little it is expected that the surface is reconstructed successfully. Then the SSE in x- and y-direction and the total SSE are calculated with the results of the last iteration step. As side-product of this step, the focal length of the concentrator is obtained with the quadratic coefficients of eq. 2.18. A result of the reconstruction with SSE is illustrated in figure 2.9.

3 Measurement Systems

Many different measurement systems are currently available on the market or under development. An extensive survey of methods is published by Arancibia-Bulnes et al. [Ara17]. Cause a flexible measurement is required some methods are not discussed in this chapter. These include methods like a tilted null screen [Ave09], analysing the flux distribution on a target[Bon18] which only provides an overall SSE as-well as pure canting methods are not considered in this work.

3.1 Laser Scanning Technique

The idea of a laser scanning set-up came up in the 1970s at Sandia Laboratories. Hansche developed a laser ray trace tester, according to the Hartmann test, for parabolic trough concentrators [Han78] called SHOT (Scanning Hartmann Optical Tester). A laser beam is reflected by a specular surface towards a Lambertian target. The position of the beam is captured by a camera. The light map is derived with the real-world coordinates of the camera and the target. The principal system set-up is presented in figure 3.1 (Further illustrations in Appendix A.1). Later Jones et al. [Jon96] developed VSHOT (Video Scanning Hartmann Optical Tester) by replacing the photo camera with a video camera. This provides higher testing speed and fewer operator interactions. The concentrator is positioned in the optical axis of the measurement system in which the laser beam orientation is horizontal. A distance of $2f$ between the vertex and the target position is recommended to achieve the most accurate results. Typically 2000 measurement points are acquired to determine the test objects surface. More data points only add little information with the cost of time [WG95]. These data points are used to calculate a best-fit approximation of the surface points relative to a perfect surface.
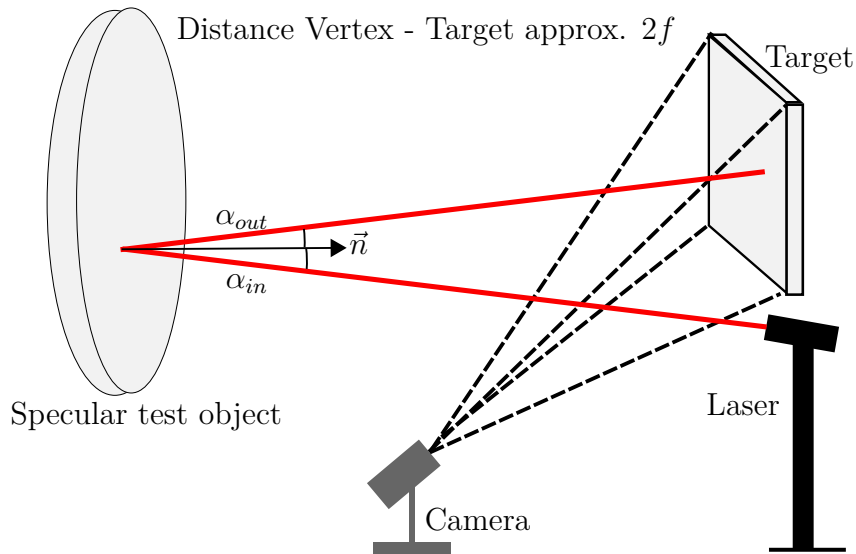
Figure 3.1: Laser Scanning Principle Setup

Before each test, the entire system needs to undergo a calibration procedure. Gray et al. [GLW10] describes the main calibration steps in table 3.1:

Calibration Step	Tool(s)
Target tilt	Bubble level
Target face to laser scanner output	Calliper
Instrument vertical offset	Human eye
Laser tilt	Inclinometer
Distance target to vertex test piece	Range finder
camera calibration	Chessboard pattern
Scanner/Calibration	Closed-loop galvanometer

Table 3.1: Calibration process for VSHOT

The largest uncertainties are caused by camera calibration and the measurement accuracy of the distance between target and vertex of the test object. The uncertainty of the entire measurement system with 95% confidence (2σ) is about $0.33mrad$. As shown this system has an enormous calibration effort before each test and requires strict positions between the system components. Measuring times from $2-5$ hours are expected for each concentrator . Furthermore, the reliability of the method decreases for larger focal length's what makes this method unsuitable for central receiver heliostats.

A similar low-cost approach of the VSHOT method is to illuminate a screen pixel by pixel. By determination which camera pixel is lit and knowledge of the related screen pixel the light map is derived as long as spatial positions of camera and screen are known. This approach was proposed by Su et al. [Su10].

An optical profilometry method proposed by Sansoni et al. [San14] is based on the same technique for parabolic trough concentrators. A shifted laser scans the test object from different locations. The SSE is obtained by the evaluation of the defocused and enlarged light spot on the target.

A close-to-series profilometry measuring method for parabolic trough facets is developed by Montecchi et al. [MBC17] and called VISprofile. VISprofile consists, according to figure 3.2, of a stationary rail with point sources and a camera mounted on a linear guide rail. The camera in figure 3.2 a) detects points S via reflection

a) Lambertian reflective point S replaces laser

b) Line of points avoid laser tilt

c) Manufactured linear guide rail
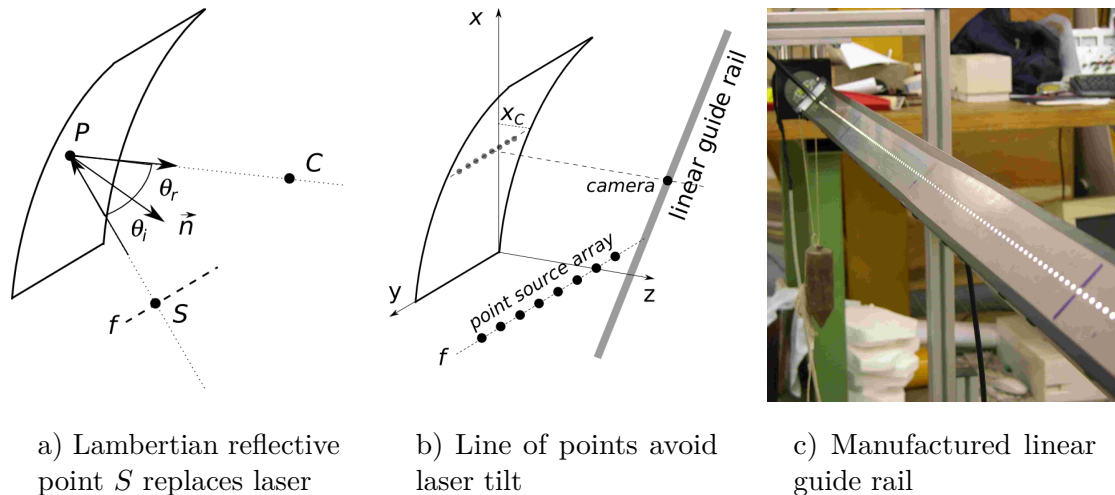
Figure 3.2: VISprofile method (Images from [MBC17])

on the screen in point P. By a repetition of Lambertian reflective points in a row with specific size and distance the tilting of the laser, compared to VSHOT, can be avoided (Figure 3.2 b and c). As no information about a starting point is installed the operator has to ensure that the entire rail is visible in the camera. Otherwise, the regularization of the inverse problem might fail. The biggest advantage of this system is, that for each line one single image is sufficient to characterize the surface slope in x- and y-direction. A precision of $20\mu rad$ and $50\mu m$ of uncertainty is measured with a measurement time of about $1min/m^2$ ($1point/cm^2$). Systems

with these properties are suitable for industrial quality controls at the end of a production line. This method could also be classified as a distant observer method in section 3.4. As the authors describe this approach as profilometry it is presented here already.

3.2 Photogrammetry

Photogrammetry combines image acquisition and processing to receive the shape and location of an object from one or more images of the object. Close-range photogrammetry is widely used for the reconstruction of three-dimensional measurements of Lambertian reflective objects. Coordinates of reference points on the test object are calculated from a series of digital pictures taken from a range of spatial positions. A reference point can be any object property which provides data like distances or geometric elements. In a first step these image points are extracted to calculate the relative orientation of two pictures. Therefore the camera intrinsic parameters described in section 2.1.2 have to be roughly estimated for a first initial value estimation. This step is applied to all captured images. Afterwards, computer vision is used to locate undefined image data in different pictures and correlate these pixels for the final multi-image triangulation. The orientated images are transferred to a global coordinate system with their calculated orientations and locations for further processing. The bundle triangulation[1] is applied to receive the point cloud of the captured object as shown in Fig 3.3. A simultaneous numerical fit approach optimizes all captured and spatially distributed images by using the reference points and estimated values of the system. This allows the software to carry out a simultaneous calibration of the camera and re-adjustment of the image locations. Each image point should be detected in at least three pictures, preferred four pictures, to solve the least bundle triangulation algorithm and obtain the relative positions of the reference points. From the finally created point cloud, the shape of the specular surface can be indirectly calculated. A high-resolution camera is required to detect and distinguish the small reference points.

---

[1]The Bundle triangulation is also called bundle block adjustment or multi-image triangulation
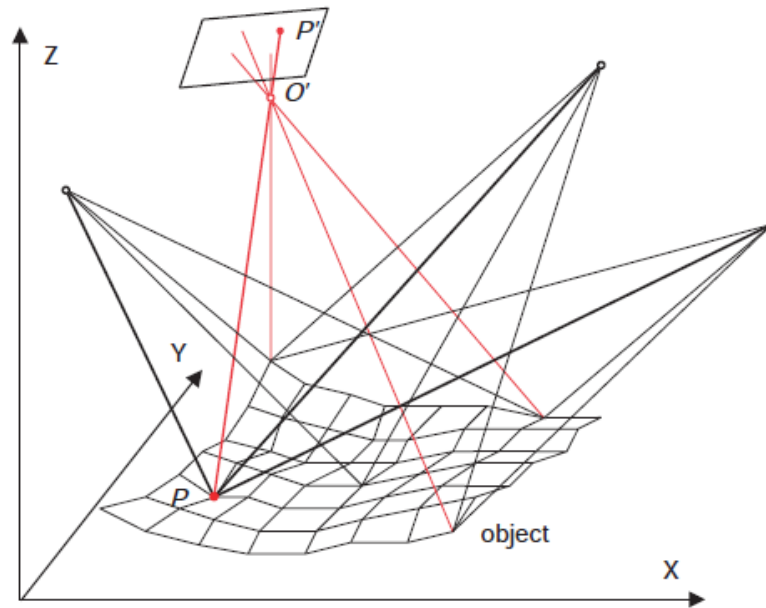
Figure 3.3: Bundle triangulation for image orientation and point determination (Image from [Luh06])

This method was first introduced in the field of solar concentrators 1997 by Shortis and Johnson [SJ97] and further developed by Pottler et al. [Pot04]. In this time photogrammetry was a rapid and inexpensive non-contact technique to characterize specular surfaces without any shape restriction. However, as the measured object has a highly specular appearance every single surface has to be prepared with reference points. These reference points have a retroreflective appearance what increases contrast and therefore the measurement accuracy. This step makes it time-consuming for characterizing entire heliostat fields (3.4). Photogrammetry is still used as an on-field measurement system to service heliostats cause of its robustness against light changing environments and simple calibration. Photogrammetry is also a standard tool to compare the results of new developed systems on its plausibility. Photogrammetry is a powerful tool to assist drone-based measurement systems. As mentioned in section 2.1.3 the accuracy for drone positions are limited to several centimetres while photogrammetry can calculate positions accurate to $0.1mm$[Luh06, p.4]. The QFly system of the DLR in chapter 3.4 makes use of this technique to identify the corner coordinates of heliostats, spatial positions of the drone for each image and the intrinsic camera parameters which are required to
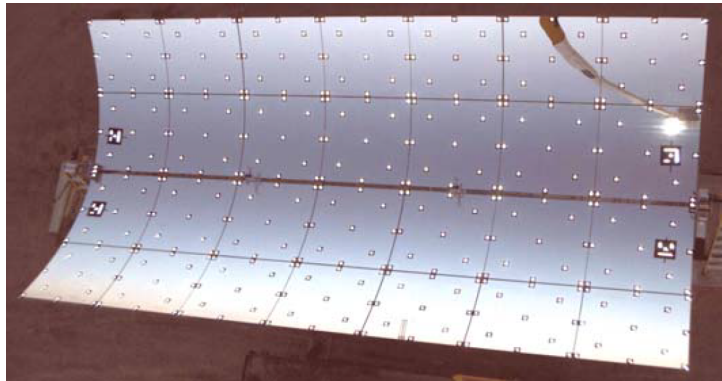
Figure 3.4: Photogrammetric setup of solar concentrator with reference points. (Image from [Pot04], p.4)

calculate the surface shape.

3.3 Deflectometry

Deflectometry systems have an equivalent measurement setup to Figure 2.2 with a screen or projector as optical emitter. The camera's view has to record the entire facet with the reflection of the image from the emitter. Deflectometry systems use a codification strategy with structured light for the light map in a way that every point of the pattern is uniquely defined. While laser scanning techniques analyse one single point in each image a deflectometry system analyses the entire facet in each image what leads to a significant reduction of images and time. An overview of developed codification strategies is published by Salvi et al. [SPB04]. Most of the systems use the periodical time-multiplexing approach, which determines the light map in a series of images. Therefore stationary positions of observer, emitter and reflector are essential. Otherwise, it is impossible to allocate the time-delayed information. Two time-multiplexing concepts are presented in 3.3.1 and 3.3.2.

With a single-shot method, it is possible to analyse dynamic motions. Therefore direct coding and spatial neighbourhood strategies are developed. Direct coding strategies with grey levels [CH85] or a coloured pattern [Gen96] are possible. Each pixel of the pattern is uniquely defined and can be allocated in the light map when detected with the camera. Theoretically, a high 3D resolution can be obtained. Practically these approaches are very sensitive to noise cause the distance and

gradient between pixel distinctions are almost zero. The other concept is based on the spatial neighbourhood and presented in 3.3.3. Each emitter pixel is uniquely defined by its surrounding pixels.

3.3.1 Binary Encoding

STERG developed 2015 an in-house deflectometry system nicknamed ZEBRA. It was developed in a shared workshop environment to characterize the shape of small heliostat facets. Space constraints and multiple light sources required a system uniquely robust against environmental changing conditions. The same approach is implemented by Butel [BSB14]. A varying binary pattern with increasing frequency is used to determine the light map. As seen in 3.5 a) the sequence of binary patterns

(a) Binary code pattern in x and y direction

(b) Evaluation of received image for one direction
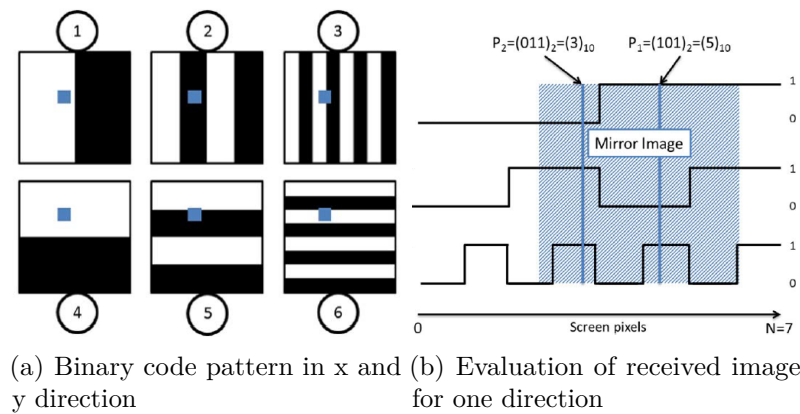
Figure 3.5: Binary encoding method (Images from [BSB14])

isolates a unique screen region. The possible screen region halves itself with each doubling of frequency. Applying this method for both directions, x and y, the pixel code for the blue square is determined ($white = 1$, $black = 0$) by eq.3.3.1:

$$pixelcode = 101101$$

The used projector has a resolution of $1920 \cdot 1080$ pixels. After formula $log_2(M) + log_2(N)$ ten images for each direction are required. To define the threshold for the boundaries one image of a white and black screen is required. This leads to a

very robust decoding stage under varying light conditions. A total of 22 images for the measurement of an entire facet are required. In comparison, a laser scanning technique would measure every single point individually which corresponds to about $2 * 10^6$ images. A significant reduction of image acquisition and processing is derived.

The frequency, and therefore the size of the region, is limited to the resolution of the projector. Another limiting factor is the image quality of the camera. The algorithm defines a threshold to distinguish between black and white areas. The borders of the patterns tend to get blurry and loose contrast which leads to a possible ambiguity of solutions.

3.3.2 Sinusoidal fringe pattern with phase shifting method

The most common deflectometry method is to apply a sinusoidal greyscale intensity modulation combined with a phase shifting method. Sandia National Laboratories developed the deflectometry system SOFAST[And13] and AIMFAST [And11] while the DLR developed the QDec-series measurement system. The QDec-M system is developed for the inspection of facets produced for CSP at the end of the production line[Ulm12]. By using multiple cameras the inverse problem can be solved after 2.2.1. This approach also allows a more compact setup as the cameras now only detect parts of the facet with overlapping areas for the regularization process. To characterize the shape of fully assembled heliostat modules in-field the DLR invented their QDec-H deflectometry system in 2011[Ulm11]. A single camera mounted on a motorized tripod with full zoom control of the lens is placed on the central tower (Figure 3.6). The required pattern is projected on a white target surface at the tower. Measurements are performed at night as light disturbances make a measurement impossible. Also, the field is not disturbed in operation mode. To analyse the images the heliostats position and angular values, which are available in an operating field, are required. This enables the system to characterize an entire heliostat field automatically in one night with uncertainties of less than $0.2mrad$ and measuring times of about $1min$ per heliostat.

The sinusoidal fringe pattern with greyscale values from $0 - 255$ requires at least
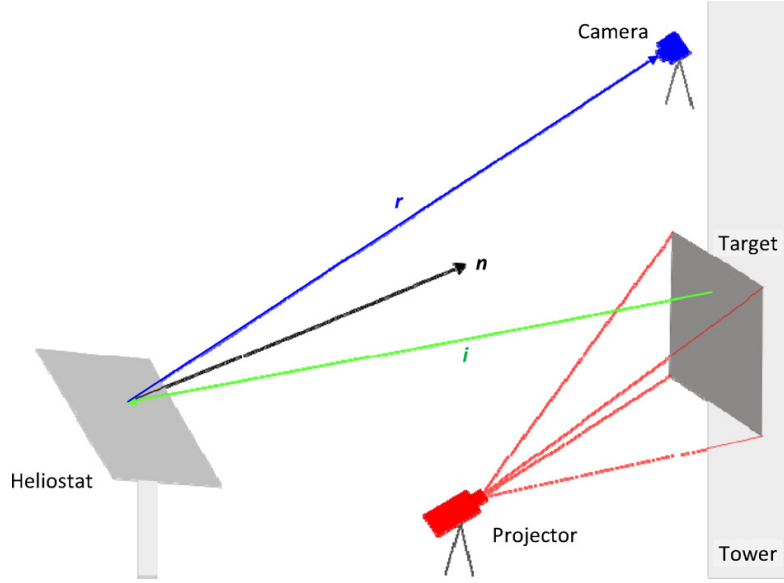
Figure 3.6: Measurement set-up used for the QDec-H System to characterize an entire heliostat field in one night (Image from [Ulm11])

three-phase shifts to determine a unique solution. Also, four or six-phase shifts are proposed to increase the stability of the method [Cre88]. The most popular variant is the four-step algorithm, also called "4-Bucket" algorithm. Phase coding is achieved by shifting the reference pattern four times by $\pi/2$[Kam05]. Figure 3.7 illustrates the shifted patterns. The brightness information $I_k(x,y)$ is described by a Fourier signal modulation for the two cases x- and y-direction:

$$I_k(x,y) = b_0(x,y) + b_1(x,y)cos\left(\phi(x,y) + k\frac{\pi}{2}\right); k = 1...4 \qquad (3.1)$$

with:

$b_0(x,y)$: temporal constant average value

$b_1(x,y)$: temporal constant amplitude.

A change of $k = k + 1$ means a phase shift of 90° (or $\pi/2$). The pattern phase $\phi(x,y)$ of each pixel, e.g. the blue pixel, is calculated from the recorded intensities $I_1(x,y)$, $I_2(x,y)$, $I_3(x,y)$ and $I_4(x,y)$ from the images:

$$\phi(x,y) = arctan\left(\frac{I_4(x,y) - I_2(x,y)}{I_1(x,y) - I_3(x,y)}\right). \qquad (3.2)$$
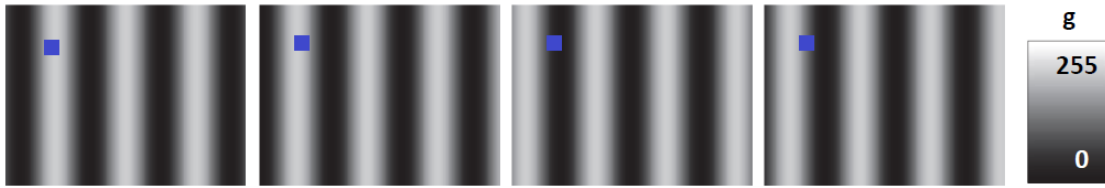
Figure 3.7: Sinusoidal fringe pattern for four step algorithm (Image from [San15, p.8])
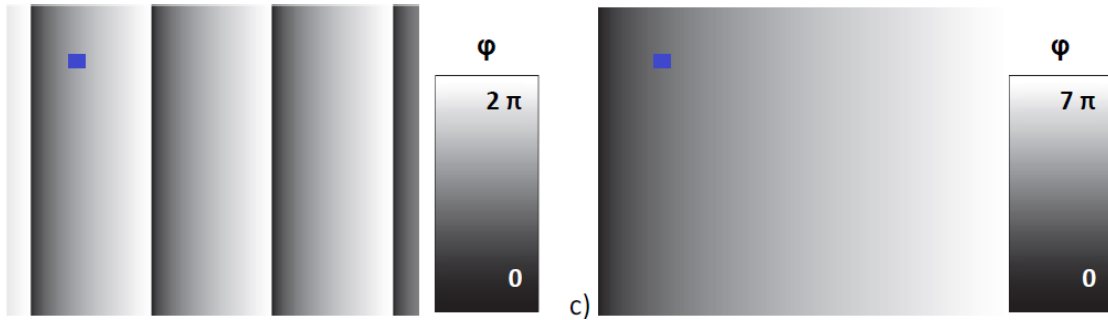
Figure 3.8: Calculated pattern phase with range $[0, 2\pi]$ (left) and unwrapped phase to solve ambiguity (right). (Image from [San15, p.8])

The calculated phase values for each pixel are illustrated in figure 3.8 (left). The result is a periodical phase value varying from $[0, 2\pi]$. Phase unwrapping is the last step to derive the final light map. This means a periodical phase value is transformed in a continuous phase distribution by systematically adding multiples of 2π. This step is illustrated in figure 3.8(right).

The advantage of sinusoidal fringe patterns to binary patterns is the achievable sub-pixel accuracy. As the sinusoidal pattern is a characteristic function of the optical system, blurred images from the camera do not affect the brightness information, only its amplitude. Blurred images furthermore have the advantage, that the discrete pattern from the projector is seen as a continuous pattern with the camera. Thus the limiting factor of the system is only dependent on the detectable grey levels of the camera.

Instead of using greyscale values Scott and Burgess [SB10] applies a coloured rainbow pattern. A region growing algorithm with the triangulation approach is chosen to solve the inverse problem and avoid a complicated unwrapping algorithm.

Initial values are available for the regularization. This approach was incorporated by students from University RWTH Aachen. In a fundamental study they describe the idea to mount this coloured pattern on the bottom of an UAV and take aerial images from the reflection of the pattern via the heliostats [Net17].

3.3.3 Spatial Neighbourhood

This kind of structured light system concentrates the entire coding information in one single pattern. The information of each point of the pattern is obtained from the neighbouring points around it. To generate these patterns different De Bruijn sequences, coloured rainbow patterns or perfect maps (M-arrays) can be used[SPB04]. Thereby the information is encoded in e.g. corners of crossing lines, structured points, grey levels and many other shapes. Two patterns are presented in figure 3.9. Curless and Seitz [CS02] developed a coloured stripe pattern with a

(a) De Bruijne sequence with coloured stripes[CS02]

(b) 2D grid with colour-coded dots[DP07]
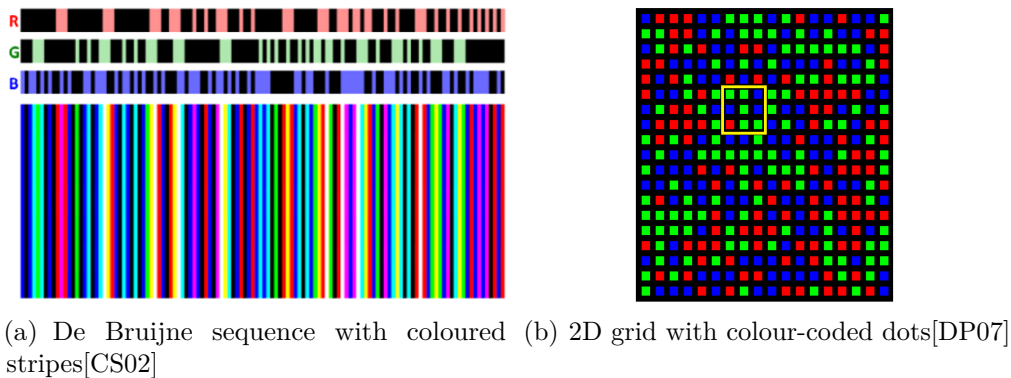
Figure 3.9: Spatial neighbourhood patterns

De Bruijn sequence in 3.9 a). A De Bruijn sequence is described with its rank n on an alphabet with size k. Thereby rank n describes the length of the codeword. This allows k^n uniquely defined codewords. In this case, five colours ($k = 5$) and the three RGB-colours describe the length of the codeword ($n = 3$). This leads to 125 codewords. There is an important constraint of all colour-indexed stripe sequences. Neighbouring stripes must have different colours as doubled stripe sizes would confuse the calculation of the light map. Pages et al. [PSM03] extended

the one-dimensional map with a colour coded sequence of vertical and horizontal slits. A two-dimensional map is received in which the cross-points of the slits are evaluated. To improve the stability of the method the decoding stage is processed in two levels. At first, cross-points which got perfectly decoded are evaluated. With the known cross-points neighbouring codewords are debugged. Almost unlimited variations of De Bruijn sequences are imaginable, e.g. Vuylsteke and Oosterlinck [VO90] developed a two-dimensional binary pattern with only two intensity levels. The two-dimensional pattern in figure 3.9 is generated with a pseudo-random array by Desjardins and Payeur [DP07] and belongs to the classification of *perfect maps*. The position of pixels is encoded in a subwindow, in this case a 3×3 subwindow (yellow), with three code words (R,G,B). With blob detection and predefined colours, the captured pattern is analysed. The centre point of each image point is finally extracted as the reflection point.

However, the decoding stage becomes more difficult and prone to errors as dependencies of each point to its neighbourhood can lead to false pattern recognition. An extensive decoding stage is required for a reliable measurement tool under changing lighting conditions. Currently, this encoding method receives little attention as the focus of development lies on stationary measurement systems. In case of a portable system these patterns might gain increasing interest due to their ability to receive the surface slope in two dimensions in one single image.

3.4 Distant Observer Method

This method uses objects around the specular reflector as an encoded pattern. Accurate knowledge about the object properties and spatial positions are required. In 2003 the first in-field measurement system, using the distant observer method, was described to characterize the CESA-I field at Plataforma Solar de Almeria[AJV03]. SCCAN (Solar Concentrator Characterization At Night) records the light of a star reflected by the reflector at night. The measurement setup is illustrated in Appendix A.2. Several heliostats can be characterized at the same time. The measurement procedure can be accelerated by analysing multiple stars. Uncertainties in slope reconstructions of about $1.0mrad$ are estimated. SCCAN is restricted through

clear nights without clouds and slow measurements for a high spatial resolution. Because of these restrictions, this method was not further developed.

For its parabolic-trough concentrators with absorber tubes the DLR particularly designed the measurement system TARMES (Trough Absorber Reflection Measurement System) ([Ulm09]). The system uses the reflection of the absorber tube as encoded pattern to calculate the surface slope of a concentrator. As the path a ray takes is reversed a ray bundle is emitted almost parallel from the absorber tube to infinity. Consequently, the further the camera is moved away from the absorber tube, the more it is enlarged in the reflection. This ensures a high sensitivity of the method. The principle is illustrated in Figure 3.4. The distance d_{cam} between
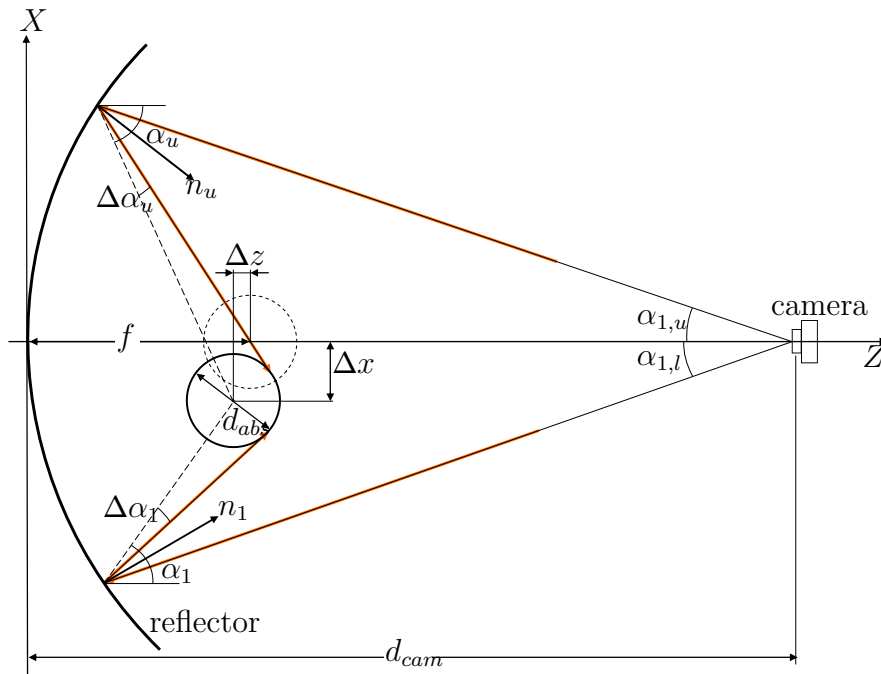
Figure 3.10: Illustration of the TARMES method. The backwards ray tracing from the camera to the absorber tube with including the possible displacement of the absorber tube (Δx, Δz) and the resulting uncertainties of $\Delta \alpha$ (Image from [Ulm09]).

camera and concentrator axis is measured with a laser distance meter as well as the deviations δx and δy of the absorber tube. The distance d_{cam} from the camera to the vertex of the concentrator should be at least $100f$. To receive realistic absorber tube deviations. The camera is placed on a tripod close to the optical axis of the
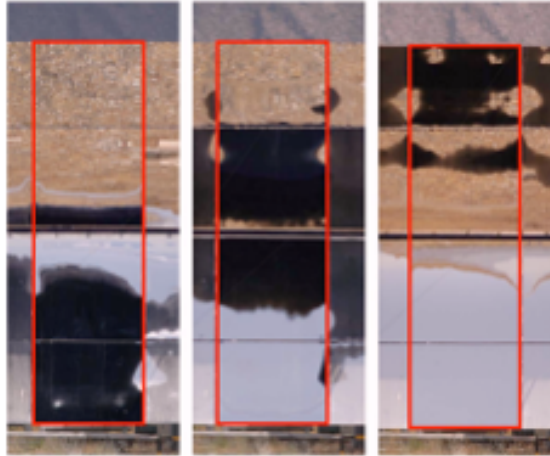
Figure 3.11: Measurement images from the TARMES system (Image from [Ulm09]).
The centred image is focusing directly into the camera. The left image is
tilting up and the right image tilting down. With the different objects in
the image (Absorber tube, sky and ground) automatized image detection
is difficult.

concentrator. During an angular motion of about 5° from the entire concentrator,
a stationary camera captures $30 - 50$ images of the reflected pattern. Each picture
has a corresponding elevation angle of the concentrator. One series of images is
illustrated in figure 3.11.

After carrying out a greyscale on each picture a line for the upper and lower
boundary of the reflected absorber tube is calculated. The surface slope is the
result of the geometrical constraints in Figure 3.4. This leads to the following
equations for the angles $\alpha_{x,u}$(upper) and $\alpha_{x,l}$(lower):

$$\alpha_{x,u} = \frac{\alpha_u + \delta\alpha_u + \alpha_{1,u}}{2}$$
$$\alpha_{x,l} = \frac{\alpha_l + \delta\alpha_l + \alpha_{l,l}}{2} \tag{3.3}$$

$$\tag{3.4}$$

It is important to mention that this method only provides information to derive
the deviations in the direction of the concentrators curvature, e.g. perpendicular
to the axis of the absorber tube. As deviations in absorber tube direction have a
subordinate impact on the optical efficiency of the power plants this is sufficient

for parabolic trough concentrators. After an edge detection algorithm detected the corners of the concentrator the surface normals are calculated. The region growing regularization is applied to calculate the surface slope. A basic uncertainty analysis is presented which shows that a maximum uncertainty of $\pm 1 mrad$ is achievable. Realistic results seem to fit in $\pm 0.2 mrad$ (RMS). Furthermore, they showed that measurements of the geometrical set-up are more critical to the results than software or camera uncertainties. Comparisons to a photogrammetric measurement show reasonable results. Further systems which use the reflection of the absorber tube are TOPCAT [DM06] and VISfield [MBE17].

2013 Prahl et al. [Pra13] advanced the TARMES measurement system and developed QFly. The first airborne measurement system for parabolic trough concentrators. QFly uses the mathematical model of figure 3.10 developed for TARMES. Here the camera is mounted on a drone what provides the superior advantage of a portable and fast measurement tool. The difference to the TARMES system is that now the observer is moving and the reflector is stationary. The drone flies above the concentrators, with a direction perpendicular to the absorber tube axis, and takes images from aerial positions. As the emitter and concentrator are one assembly the camera is not restricted to specific image capturing positions. This allows the first time a fast measurement of the concentrator in operating mode. As a result of a moving camera, new issues emerge. Major challenges of the new design are unknown positions of the camera relative to the concentrators, camera calibration, image quality and hardware restrictions. Drones have restricted payloads and flight times. Wind speeds below $6m/s$ can be tolerated without significant influence on the measurement result while gusts cause a sudden movement of the camera and therefore lower image quality. To avoid blurring of images the camera requires short exposure times below $0.5ms$. A precise determination of the drone position is substantial for an accurate system. As described in section 2.1.3 the highest achievable accuracy with an advanced RTK-GPS system is of several centimetres. This doesn't fulfil the accuracy requirements of a measurement system for high-performance applications. The solution is to use the photogrammetry approach from section 3.2. This ensures the correct drone positions of each image relative to the concentrators. The spatial positions of the concentrator corners are required. Additional retroreflective coded markers, placed on the concentrators, are used to
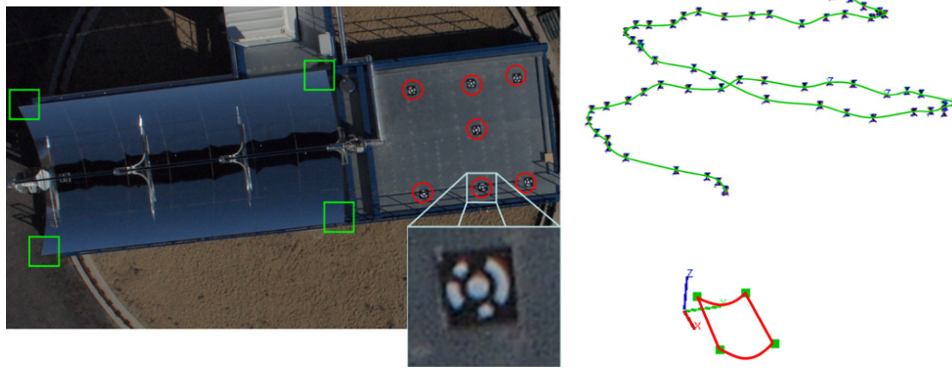
(a) Image with corner detection and detected retroreflective markers for optimized bundle adjustment

(b) Derived camera positions relative to the concentrator in a Cartesian coordinate system

Figure 3.12: Photogrammetric image and result(Images from [Pra13])

optimize the bundle adjustment. This is illustrated in figure 3.12 a).

The photogrammetry system provides the camera distortion parameters of the camera lens. This side-product of photogrammetry is of high importance as it allows an automated evaluation of the images. A result of the photogrammetric output is illustrated in figure 3.12 b). The camera positions are calculated relative to the concentrator in a Cartesian coordinate system. Largest impact on the measurement inaccuracies of TARMES are the geometrical uncertainties. The photogrammetric approach allows an optimized calculation of the absorber tube and thereby the displacements Δx and Δz[Pra17]. The absorber tube is located accurately to $1,5mm$ in x- and z-direction. A Monte Carlo ray trace simulation indicates an absolute measurement uncertainty of about $\pm 0.1 mrad$ (RMS). Current developments aim in a completely autonomous measurement tool. Therefore the retroreflective targets should be avoided by implementation in the image analysis process. First experiments with edge detection in 2008 did not lead to sufficient accuracies[RPU08].

A novel method is developed by [CCH17; CHC18] to receive geometrical aberrations of heliostats with point focus. Images of the heliostat showing the reflection of the sun are taken from different points of view. With a known sun intensity profile it is possible to reconstruct the surface. This method uses the sun's limb-darkening
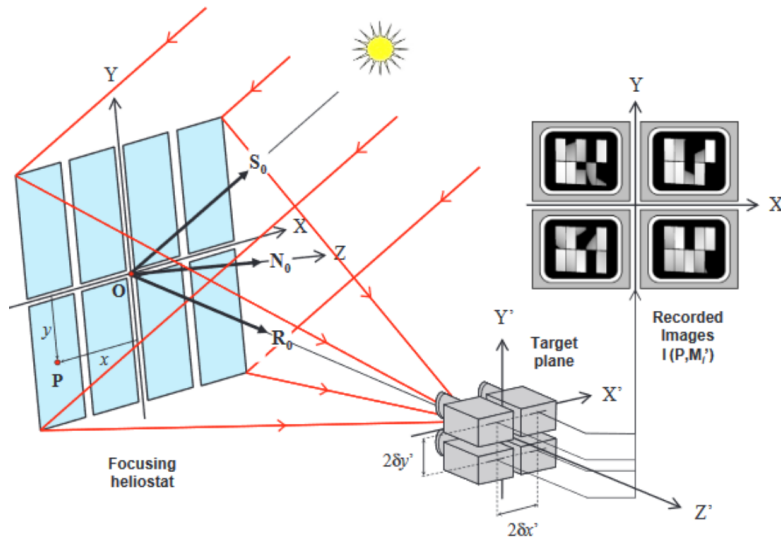
Figure 3.13: Priniciple of backward-gazing method (Image from [CHC18])
Distances between the cameras are well known with $\delta x'$ and $\delta y'$. They define the measurement distance to the specular surface. E.g. $\delta x'$ and $\delta y'$ were set to $200mm$ for a focusing distance around $100m$[Hén18]. Precise alignment of the cameras is crucial for the reconstruction of the surface.

appearance. The intensity of the sun profile decreases with increasing distance to the centre. In general, this can be expressed by a Super Gaussian profile. This encryption is similar to the phase shift method of deflectometry. Cause of the rotationally symmetric intensity distribution of the assumed sun profile at least three points of views are required to solve the ambiguity of circles with constant intensities. if four points of view are considered an increased stability of the method is achieved. This case is illustrated in figure 3.13. For highest accuracies the four cameras are placed close to the central receiver where they approx. have a distance of the focal length f to the heliostats. Surface slopes are received from heliostats in operating mode, previously only possible with the QFly system for parabolic trough systems[2]. Under real-world conditions, interactions of the sunlight in the atmosphere has an impact on the sun profile received at the ground. As the sun profile includes the encoded pattern in the form of the intensity distribution this has a large impact on the measurement reliability and accuracy. To adjust this issue a fifth camera is installed in the measurement set-up which captures the sun

---

[2]With some limitations it is also possible with the SCCAN system for designed for heliostats.

profile and analyses the intensity distribution.

This method provides optical and mechanical errors of heliostats. The precision of the system is estimated to be around $0.05mrad$ (RMS) for SSE and $5\mu m$. However, this method is very sensitive to image noise. Simulations show that noise due to the heat of a stationary camera has a significant impact on the results.

3.5 Specular Flow

Reconstruction methods for specular surfaces usually require a well-known emitter shape and location. If this is not available optical flow provides solutions for unknown environments[3]. This approach is based on the motion of observer and environment relative to the reflector. It is possible to recover parts of a specular surface by tracking a single environmental feature over a series of images during camera motion. It is important to mention explicitly that this method only uses specular flow, this means no a-priori knowledge about the environment is required as used for the distant observer method. The main problem of this approach is an accurate computation of optical flow which is an ill-posed problem by itself[HS93]. Specular flow is explicitly defined at curved surface points. For surface points with curvature equals zero, or close to zero, so called parabolic singularities appear. Adato et al. [AZB10] explain this with a drastically growing magnitude of specular flow as surface curvature decreases. These parabolic singularities are significantly more difficult to detect than common singularities which occur at surface boundaries. Here singularities can occur everywhere on the test object what makes it harder to detect, trace and handle them. Different approaches with assumptions are presented. 2006 Roth and Black [RB06] have investigated specular flow with diffuse and specular components. A model is generated to recover a specular sphere covered by some diffuse markers with a moving environment. They could prove that specular flow provides information for surface reconstructions. Adato et al. [Ada07] assumes a moving, unknown far-field environment and a stationary observer. To simplify the reconstruction problem the environment and observer are assumed to be far away from the specular surface. This simplifies the environment motion field

---

[3]Emitter is called environment for specular flow

into a function of only two angles as the distant parameters vanish. This approach is illustrated in figure 3.14.
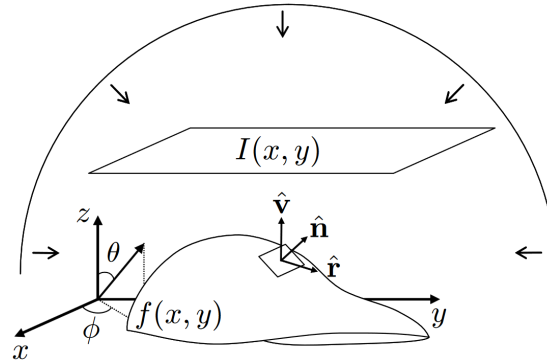
Figure 3.14: Specular shape reconstruction problem in three dimensions with far-field illumination (Image from [Ada07]). The two angles ϕ and θ describe a point of the far-field illumination sphere. The image plane $I(x, y)$ is orthogonal to the xy-plane.

A system of coupled non-linear partial differential equations is obtained to solve the reconstruction with initial conditions from the object boundaries. Further related investigations are presented by [ON97], [Ada10],[AS11] and [Li14]. These frameworks are still on a theoretical level with proof of concepts.

3.6 Evaluation of operational measurement systems

A survey of measurement systems, mostly stationary systems, is given in this chapter. Presented are optical measurement set-ups for the characterization of concentrator SSE. Table 3.2 illustrates a brief overview of the different measurement systems targeting reflector type, precision, status of the test object and general restrictions. The table shows very clear that present in-field characterization of solar concentrators is utilized with *Distant Observer Methods*. With *Specular Flow* a high research effort is aiming to improve this method towards a more flexible and independent model.

System		Reflector type(s)[4]	Uncertainty RMS [mrd]	Test object position	In-field	Restrictions
Laser Scanning	VSHOT	Parabolic Trough	0.33	Dependent	Yes	Short focal lengths, calibration
Profilometry	VISprofile	Parabolic Trough	0.02	Dependent	No	Length of emitter rail
Photogrammetry		Everything	0.02 - 0.05	Free	Yes	Preparation, indirect measurement (height profile)
Deflectometry	QDec-H[5]	Heliostat	0.2	Dependent	Yes	stationary observer and emitter
Distant Observer Method	SCCAN	Heliostat	1	Dependent	Yes	Only at night, imprecise
	TARMES	Parabolic Trough	0.2	Dependent	Yes	Absorber tube, one-dimensional results
	QFly	Parabolic Trough	0.1	Free	Yes	
	Backward-Gazing	Heliostat	0.05	Tracking	Yes	Noise sensitive, sun visibility

Table 3.2: Overview of operational measurement systems

To the best of the author's knowledge, there is no portable or drone-based measurement system designed for the in-field characterization of heliostats SSE. However, analysing currently operational measurement systems, the previously investigated measurement systems have similar fundamental requirements:

1. Design unambiguous pattern which leads to *simple light map*
2. Receive spatial positions of system objects relative to each other (Emitter, observer and if required initial points of concentrator)
3. Analyse images to receive *light map*
4. Regularization of the *Inverse Problem*
5. Reconstruction of concentrator spatial position and orientation
6. Calculate SSE

---

[4]The theoretical possibility to extend the system's capability of measuring additional concentrator types is not considered in this table.

[5]Other deflectometric systems are SOFAST, AIMFAST or the QDec-M system. These systems give similar results but only operate in a controlled environment.

Transferring these requirements to a drone-based measurement system, for the characterization of heliostats, different constraints occur. While steps 3-6 are software based and already well investigated the first two steps are based on physical appearances. Under the assumption that no field preparations are allowed the first two steps require deeper analysis. A statement about the feasibility of a drone-based measurement system for heliostats SSE highly depends on their technical practicability.

Design of pattern

In contrast to stationary measurement systems, the observer is moving on a drone-based system. As no field preparations are allowed the pattern needs to be mounted on the drone.

Laser scanning techniques are only precise for short focal lengths of the concentrator. Therefore they are not viable for the measurement of heliostats.

To apply the time-multiplexing approach from deflectometric systems the information from the emitter needs to jump a defined step[6]. It is very unlikely to get the perfect timing for this requirement.

Distant Observer Methods use accurate knowledge of the shape and spatial positions from components which are naturally present around a solar field. TARMES and QFly utilizes the absorber tube as pattern to analyse the shape of Parabolic Trough concentrators. The advantage of this system is the physical segregation of the absorber tube as a pattern and the camera. Because of the moving observer, it is possible to measure the concentrator shape in different orientations. This setup allows the collection of large data amounts with a single flight over the test object. Heliostats do not provide such a component. For a direct adaptation of the system, it would be required to mount a tube on the drone. Figure 3.15 a) gives a schematic illustration of this possible setup.

With the direct connection of camera and tube, the heliostats orientation is strictly dependent and needs to focus roughly parallel to the tube axis direction. Straight lines only provide one-dimensional information. Heliostats are designed for point focus and therefore a two-dimensional shape needs to be measured. Consequently two measurements in perpendicular directions are required to analyse the shape of

---

[6]Depends on the chosen number of phase shifts for the image processing and evaluation

(a) Tube mounted on a drone (TARMES adaption)

(b) Perfect maps with single shot results
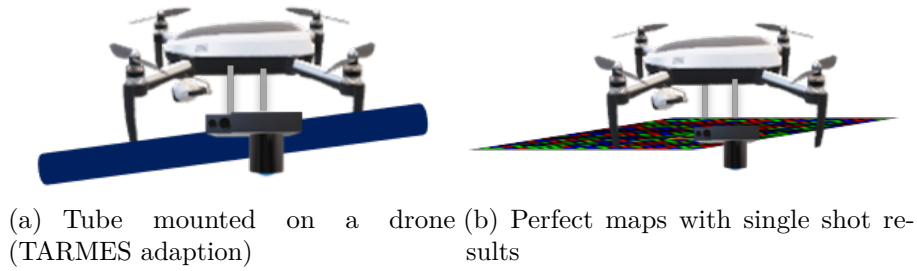
Figure 3.15: Schematic setup of measurement principles adapted for heliostats

heliostats. Furthermore, the TARMES system provides high sensitivity by magnifying the absorber tube in the solar concentrator. This is not given for heliostats due to the same distance of tube and camera towards the heliostat under the prevalent conditions.

The backward-gazing method uses the sun profiles intensity distribution as a pattern. Information is stored in tiny changes of intensity levels. Optimal image capturing conditions are required. Drone operated cameras are continuously moving and shaking. Suboptimal image capturing conditions lead to blurry images and changes in the optical system of the camera. It is very unlikely to get a robust decoding stage for this pattern.

Under the given conditions with moving observer and changing environments, it is challenging to develop a reliable automated decoding stage. A robust image processing stage with a following debugging is required for good results. One possible way to ensure a robust decoding stage is by increasing the distance and gradient between distinctive features of the pattern. A selection of possible patterns are described in section 3.3.3. The given example with perfect maps only requires three different features: Red, green and blue. These maps are limited to clear allocation of codewords by the usage of colours and subwindow size. In contrast, they provide two-dimensional information and results in a single shot. Figure 3.15 b) might be a possible solution to receive highly accurate knowledge of various concentrator shapes. The here proposed set-up can be seen as an extension of the pattern of the operating system *VISprofile*. Each point of the pattern is retraceable to its origin.

The limitation of codewords can possibly be avoided by stitching multiple images together.

Spatial positions of components

Stationary measurement systems often use laser distance meters which provide sufficient information about spatial positions for most applications. Other systems use a multi-camera regularization approach to avoid accurate knowledge about the position of the concentrator and utilize advanced algorithms to identify possible surface points. In a system with independent camera positions, a successful implementation of laser distance meters leads to high motion control requirements. Drones usually have an inbuilt GPS. The highest accessible accuracies for drone positioning with the RTK-GPS lies within several cm's. It is very unlikely that this is sufficient for measurement accuracies below $0.2 mrad$ RMS. The QFly system implemented photogrammetry to solve this problem. This results in two major advantages: Photogrammetry delivers very accurate results about spatial positions and provides the camera's internal parameters. To guarantee a reliable operation photogrammetry requires additional retroreflective targets around and on the solar concentrators to operate. Present developments to avoid these markers are not reliable or accurate enough for automatized applications. Without photogrammetry, a complex camera calibration must be performed before each measurement flight on the cost of time and resources.

4 Conclusion

This work investigates the theoretical feasibility of measuring surface slope errors of heliostats using UAVs. To the best of the authors' knowledge, there is currently no system on the market to identify heliostats surface slope errors using a drone. A measurement system which operates from a drone completely independent from the solar field, under changing lighting, seems to be achievable after working on this study. In contrast, it seems to be very difficult to execute measurements of heliostats in different operation modes without any field preparations.

We started this thesis by introducing the required tools and mathematical concepts to derive the shape from specular reflection. This includes the hardware components consisting of camera and UAV as well as the software side including the inverse problem, regularization of the inverse problem and the surface reconstruction from gradient data. Afterwards, we categorized and analysed the operational measurement systems which are currently used to identify the SSE of various concentrators for solar thermal power plants. Current research focuses on the Distant Observer Method to analyse parabolic trough concentrators. Utilizing standardized features which occur naturally in or around solar fields is a cost-effective and flexible solution to characterize the shape of concentrators. With enough computation power and further research, the field *Specular Flow* could derive concentrator shapes only using a single camera. But these frameworks are still on a theoretical level and far away from industrial applications.

A general procedure for the optical measurement of concentrators including six steps was detected. The crucial steps for an UAV-based in-field measurement system are: Choosing a suitable codification strategy and receiving the spatial positions of system components. An unambiguous codification strategy is required which is robust against lighting changes and contains sufficient information for

surface reconstruction of heliostats. Patterns belonging to the group of *Spatial Neighbourhood* seem to provide reliable robustness against lighting changes if an extensive debugging stage follows the decoding stage. Combined with photogrammetry a flexible and robust measurement system could be achieved.

Each technology by itself, which is required to build an UAV-based measurement system, is available and meets the demands. A complicated UAV-based measurement system needs to connect these technologies in a very efficient way. Technologies and methods have to be adapted for this purpose. Photogrammetry may be the central tool to allow cost-effective measurements taken from UAVs. Providing spatial positions and internal parameters without adding hardware to the measurement system. Thus it is a lot more powerful than expected at the beginning of this thesis. In a first step, a suitable codification strategy should be chosen and tested in a lab environment. Further investigations should also target the availability of photogrammetry software, preferably open source.

With QFly the DLR proofed that it is possible to create an aerial measurement system to characterize the shape of solar concentrators with high speed and precision. Thus we are confident to find a flexible solution to characterize heliostats from a drone as well.

Bibliography

[Sol18]   SolarPACES. *How CSP Works: Tower, Trough, Fresnel or Dish.* SolarPACES. June 2018. url: https://www.solarpaces.org/how-csp-works/.

[Bar15]   J. Barbee. *South African team may have solved solar puzzle even Google couldn't crack.* The Guardian. Aug. 2015. url: https://www.theguardian.com/environment/2015/aug/24/south-african-team-may-have-solved-solar-puzzle-even-google-couldnt-crack.

[LS12]   K. Lovegrove and W. Stein. *Concentrating solar power technology: principles, developments and applications.* Elsevier, 2012.

[Bla11]   M. Blanco, A. Mutuberria, A. Monreal, and R. Albert. "Results of the empirical validation of Tonatiuh at Mini-Pegase CNRS-PROMES facility". In: *SolarPACES* (2011).

[Mei14]   S. Meiser, E. Lüpfert, B. Schiricke, and R. Pitz-Paal. "Analysis of Parabolic Trough Concentrator Mirror Shape Accuracy in different Measurement Setups". In: *Energy Procedia* 49 (2014). Proceedings of the SolarPACES 2013 International Conference, pp. 2135–2144. issn: 1876-6102. doi: https://doi.org/10.1016/j.egypro.2014.03.226.

[TD91]   H. Tagare and R. DeFigueiredo. "A Theory of Photometric Stereo for a Class of Diffuse Non-Lambertian Surfaces". In: *Pattern Analysis and Machine Intelligence, IEEE Transactions on* 13 (Mar. 1991), pp. 133–152. doi: 10.1109/34.67643.

[Kam05]   S. Kammel. "Deflektometrische Untersuchung spiegelnd reflektierender Freiformflächen". German. PhD thesis. 2005. 115 pp. isbn: 3-937300-28-7. doi: 10.5445/KSP/1000002980.

[Luh06]   T. Luhmann, S. Robson, S. Kyle, and I. Harley. *Close Range Pho-togrammetry: Principles, Techniques and Applications.* Jan. 2006. isbn: 9780470106334.

[Bra00]   G. Bradski. "The OpenCV Library". In: *Dr. Dobb's Journal of Software Tools* (2000).

[BLF12]   J. Beyerer, F. León, and C. Frese. *Automatische Sichtprüfung.* Springer Berlin Heidelberg, Oct. 22, 2012. isbn: 978-3-642-23966-3.

[RGM16]   B. Rao, A. Gopi, and R. Maione. "The societal impact of commercial drones". In: *Technology in Society* 45 (May 2016), pp. 83–90. doi: 10.1016/j.techsoc.2016.02.009.

[Ghe15]   D. Gheorghiţă, I. Vîntu, L. Mirea, and C. Brăescu. "Quadcopter control system". In: *2015 19th International Conference on System Theory, Control and Computing (ICSTCC).* Oct. 2015, pp. 421–426. doi: 10.1109/ICSTCC.2015.7321330.

[Nor08]   Z. Nordin, M. Yahya, W. Mohd Akib, W. Aziz, and Z. Mat Amin. "The utilization of RTK-GPS for real-time structural health detection". In: May 2008.

[BW10]   J. Balzer and S. Werling. "Principles of Shape from Specular Reflec-tion". In: *Measurement* 43 (Dec. 2010), pp. 1305–1317. doi: 10.1016/j.measurement.2010.07.013.

[RC01]   S. Rahmann and N. Canterakis. "Reconstruction of specular surfaces using polarization imaging". In: *Proceedings of the 2001 IEEE Computer Society Conference on Computer Vision and Pattern Recognition. CVPR 2001.* Vol. 1. Dec. 2001, pp. I–I. doi: 10.1109/CVPR.2001.990468.

[Tar05]   M. Tarini, H. Lensch, M. Goesele, and H. Seidel. "3D acquisition of mirroring objects using striped patterns". In: *Graphical Models* 67.4 (2005), pp. 233–259. issn: 1524-0703. doi: https://doi.org/10.1016/j.gmod.2004.11.002.

[Rap12]   H. Rapp. "Reconstruction of Specular Reflective Surfaces using Auto-Calibrating Deflectometry". PhD thesis. 2012.

[KKH04]   M. Knauer, J. Kaminski, and G. Häusler. "Phase Measuring Deflectometry: a new approach to measure specular free-form surfaces". In: *Proceedings of SPIE - The International Society for Optical Engineering* 5457 (Sept. 2004). doi: 10.1117/12.545704.

[SB10]   P. Scott and G. Burgess. "Measurement of Mirror Panels Using Coloured Pattern Deflectometry". In: 2010.

[Hor07]   J. Horbach. "Verfahren zur optischen 3D-Vermessung spiegelnder Oberflächen". German. PhD thesis. 2007. 120 pp. isbn: 978-3-86644-202-3. doi: 10.5445/KSP/1000007348.

[Ara17]   C. Arancibia-Bulnes, M. Peña-Cruz, A. Mutuberría, R. Uribe, and M. Sánchez. "A survey of methods for the evaluation of reflective solar concentrator optics". In: *Renewable and Sustainable Energy Reviews* 69 (Mar. 2017), pp. 673–684. doi: 10.1016/j.rser.2016.11.048.

[Ave09]   M. Avendaño-Alejo, V. Moreno-Oliva, M. Campos-García, and R. Díaz-Uribe. "Quantitative evaluation of an off-axis parabolic mirror by using a tilted null screen". In: *Appl. Opt.* 48.5 (Feb. 2009), pp. 1008–1015. doi: 10.1364/AO.48.001008.

[Bon18]   A. Bonanos, M. Faka, D. Abate, S. Hermon, and M. Blanco. "Optical characterization of heliostats using multiple 3D geometry characterization sensors". In: *AIP Conference Proceedings* 2033.1 (2018), p. 040008. doi: 10.1063/1.5067044.

[Han78]   B. Hansche. "Laser Ray Trace Tester for Parabolic Trough Solar Collectors". In: *NDT Technology Division 9352, Sandia Laboratories, New Mexiko* (1978).

[Jon96]   S. Jones, D. Neal, J. Gruetzner, R. Houser, R. Edgar, and T. Wendelin. "VSHOT: a tool for characterizing large, imprecise reflectors". In: Nov. 1996.

[WG95]   T. Wendelin and J. Grossman. "Comparison of three methods for optical characterization of point-focus concentrators". In: *Solar Energy* -1 (Feb. 1995), pp. 19–24.

[GLW10]   A. Gray, A. Lewandowski, and T. Wendelin. *Video Scanning Hartmann Optical Tester (VSHOT) Uncertainty Analysis (Milestone Report)*. Tech. rep. National Renewable Energy Laboratory (NREL), Oct. 2010. url: digital.library.unt.edu/ark:/67531/metadc1013504/.

[Su10]   P. Su, R. Parks, L. Wang, R. Angel, and J. Burge. "Software configurable optical test system: a computerized reverse Hartmann test". In: *Appl. Opt.* 49.23 (Aug. 2010), pp. 4404–4412. doi: 10.1364/AO.49.004404.

[San14]   P. Sansoni, D. Fontani, L. Mercatelli, D. Jafrancesco, E. Sani, S. Coraggia, M. Meucci, L. Marconi, and S. Toccafondi. "Mirror Surface Check on Solar Troughs by Optical Profilometry". In: *Energy Procedia* 57 (2014). 2013 ISES Solar World Congress, pp. 2819–2827. issn: 1876-6102. doi: https://doi.org/10.1016/j.egypro.2014.10.315.

[MBC17]   M. Montecchi, A. Benedetti, and G. Cara. "Fast 3D Optical-Profilometer for the Shape-Accuracy Control of Parabolic-Trough Facets". In: 2017.

[SJ97]   M. Shortis and G. Johnston. "Photogrammetry: An Available Surface Characterization Tool for Solar Concentrators, Part II: Assessment of Surfaces". In: *Journal of Solar Energy Engineering* 2 (Nov. 1997), pp. 286–291. doi: 10.1115/1.2888034.

[Pot04]   K. Pottler, E. Lüpfert, G. Johnston, and M. Shortis. "Photogrammetry: A Powerful Tool for Geometric Analysis of Solar Concentrators and Their Components". In: vol. 127. July 2004. doi: 10.1115/1.1824109.

[SPB04]   J. Salvi, J. Pagès, and J. Batlle. "Pattern codification strategies in structured light systems". In: *Pattern Recognition* 37 (2004), pp. 827–849.

[CH85]   B. Carrihill and R. Hummel. "Experiments with the intensity ratio depth sensor". In: *Computer Vision, Graphics, and Image Processing* 32.3 (1985), pp. 337–358. issn: 0734-189X. doi: https://doi.org/10.1016/0734-189X(85)90056-8.

[Gen96]   Z. Geng. "Rainbow three-dimensional camera: New concept of high-speed three-dimensional vision systems". In: *Optical Engineering - OPT ENG* 35 (Feb. 1996), pp. 376–383. doi: 10.1117/1.601023.

[BSB14]   G. Butel, G. Smith, and J. Burge. "Binary pattern deflectometry". In: *Appl. Opt.* 53.5 (Feb. 2014), pp. 923–930. doi: 10.1364/AO.53.000923.

[And13]   C. Andraka, S. Sadlon, B. Myer, K. Trapeznikov, and C. Liebner. "Rapid Reflective Facet Characterization Using Fringe Reflection Techniques". In: *Journal of Solar Energy Engineering* 136 (Apr. 2013). doi: 10.1115/ES2009-90163.

[And11]   C. Andraka, J. Yellowhair, K. Trapeznikov, J. Carlson, B. Myer, B. Stone, and K. Hunt. "AIMFAST: An Alignment Tool Based on Fringe Reflection Methods Applied To Dish Concentrators". In: *Journal of Solar Energy Engineering* 133.3 (July 2011), pp. 031018–031018-6. issn: 0199-6231. doi: 10.1115/1.4004357.

[Ulm12]   S. Ulmer, C. Weber, H. Koch, M. Schramm, H. Pflüger, P. Climent, and H. Yildiz. "High-Resolution Measurement Sysem for Parabolic Trough Concentrator Modules in Series Production". In: *Solar Energy* (2012). Proceedings of Solar PACES Conference Marrakech, Morocco.

[Ulm11]   S. Ulmer, T. März, C. Prahl, W. Reinalter, and B. Belhomme. "Automated high resolution measurement of heliostat slope errors". In: *Solar Energy* 85.4 (2011). SolarPACES 2009, pp. 681–687. issn: 0038-092X. doi: https://doi.org/10.1016/j.solener.2010.01.010.

[Cre88]   K. Creath. "V phase-measurement interferometry techniques". In: *Progress in optics*. Vol. 26. Elsevier, 1988, pp. 349–393.

[San15]   M. Sandner. "Optical measurement of partially specular surfaces by combining pattern projection and deflectometry techniques". PhD thesis. Jan. 2015. doi: 10.13140/RG.2.1.3771.7363.

[Net17]   L. Netze, J. Theissen, P. Peltzer, and A. Niebrügge. "Detecting Deformations of Heliostat Surfaces Using Deflectometry with Drones". In: RWTH Aachen, Oct. 2017.

[CS02]   B. Curless and S. Seitz. "Rapid shape acquisition using color structured light and multi-pass dynamic programming". In: *Proceedings. First International Symposium on 3D Data Processing Visualization and Transmission*. June 2002, pp. 24–36. doi: 10.1109/TDPVT.2002.1024035.

[DP07]   D. Desjardins and P. Payeur. "Dense Stereo Range Sensing with March-
           ing Pseudo-Random Patterns". In: *Fourth Canadian Conference on
           Computer and Robot Vision (CRV '07)*. May 2007, pp. 216–226. doi:
           10.1109/CRV.2007.22.

[PSM03]   J. Pages, J. Salvi, and C. Matabosch. "Robust Segmentation and Decod-
           ing of a Grid Pattern for Structured Light". In: June 2003, pp. 689–696.
           doi: 10.1007/978-3-540-44871-6_80.

[VO90]   P. Vuylsteke and A. Oosterlinck. "Range image acquisition with a
           single binary-encoded light pattern". In: *IEEE Transactions on Pattern
           Analysis and Machine Intelligence* 12.2 (Feb. 1990), pp. 148–164. issn:
           0162-8828. doi: 10.1109/34.44402.

[AJV03]   F. Arqueros, A. Jiménez, and A. Valverde. "A novel procedure for the
           optical characterization of solar concentrators". In: *Solar Energy* 75.2
           (2003), pp. 135–142. issn: 0038-092X. doi: https://doi.org/10.1016/j.
           solener.2003.07.008.

[Ulm09]   S. Ulmer, B. Heinz, K. Pottler, and E. Lüpfert. "Slope Error Mea-
           surements of Parabolic Troughs Using the Reflected Image of the Ab-
           sorber Tube". In: *Journal of Solar Energy Engineering* (2009). doi:
           10.1115/1.3035811. url: http://dx.doi.org/10.1115/1.3035811.

[DM06]   R. Diver and T. Moss. "Practical Field Alignment of Parabolic Trough
           Solar Concentrators". In: *Journal of Solar Energy Engineering* 129.2
           (June 2006), pp. 153–159. issn: 0199-6231. doi: 10.1115/1.2710496.

[MBE17]   M. Montecchi, A. Benedetti, and G. Emiliano La Cara. "Optical align-
           ment of parabolic trough modules". In: 2017.

[Pra13]   C. Prahl, B. Stanicki, C. Hilgert, S. Ulmer, and M. Röger. "Airborne
           shape measurement of parabolic trough collector fields". In: *Solar Energy*
           91 (2013), pp. 68–78. issn: 0038-092X. doi: https://doi.org/10.1016/j.
   solener.2013.01.012.

[Pra17] C. Prahl, M. Röger, B. Stanicki, and C. Hilgert. "Absorber tube displacement in parabolic trough collectors – A review and presentation of an airborne measurement approach". In: *Solar Energy* 157 (2017), pp. 692–706. issn: 0038-092X. doi: https://doi.org/10.1016/j.solener.2017.05.023.

[RPU08] M. Röger, C. Prahl, and S. Ulmer. "Fast Determination of Heliostat Shape and Orientation by Edge Detection and Photogrammetry". In: Mar. 2008.

[CCH17] M. Coquand, C. Caliot, and F. Hénault. "Backward-gazing method for heliostats shape errors measurement and calibration". In: *AIP Conference Proceedings* 1850.1 (2017), p. 030010. doi: 10.1063/1.4984353.

[CHC18] M. Coquand, F. Henault, and C. Caliot. "Numerical identification of mirror shapes with the backward-gazing method using an actual solar profile". In: *AIP Conference Proceedings* 2033.1 (2018), p. 040010. doi: 10.1063/1.5067046.

[Hén18] F. Hénault, M. Coquand, P. Defieux, and C. Caliot. "Sun backward gazing method with multiple cameras for characterizing solar concentrators". In: *Solar Energy* 166 (2018), pp. 103–114. issn: 0038-092X. doi: https://doi.org/10.1016/j.solener.2018.03.042.

[HS93] B. Horn and B. Schunck. ""Determining optical flow": a retrospective". In: *Artificial Intelligence* 59.1 (1993), pp. 81–87. issn: 0004-3702. doi: https://doi.org/10.1016/0004-3702(93)90173-9. url: http://www.sciencedirect.com/science/article/pii/0004370293901739.

[AZB10] Y. Adato, T. Zickler, and O. Ben-Shahar. "Toward robust estimation of specular flow". In: Jan. 2010, pp. 1–11. doi: 10.5244/C.24.22.

[RB06] S. Roth and M. Black. "Specular Flow and the Recovery of Surface Structure". In: vol. 2. Jan. 2006, pp. 1869–1876. doi: 10.1109/CVPR.2006.290.

[Ada07] Y. Adato, Y. Vasilyev, O. Ben-Shahar, and T. Zickler. "Toward a Theory of Shape from Specular Flow". In: Nov. 2007, pp. 1–8. isbn: 978-1-4244-1631-8. doi: 10.1109/ICCV.2007.4408883.

[ON97]   M. Oren and S. Nayar. "A Theory of Specular Surface Geometry". In: *Int. J. Comput. Vision* 24.2 (Sept. 1997), pp. 105–124. issn: 0920-5691. doi: 10.1023/A:1007954719939. url: https://doi.org/10.1023/A: 1007954719939.

[Ada10]   Y. Adato, Y. Vasilyev, T. Zickler, and O. Ben-Shahar. "Shape from Specular Flow". In: *Pattern Analysis and Machine Intelligence, IEEE Transactions on* 32 (Dec. 2010), pp. 2054–2070. doi: 10.1109/TPAMI. 2010.126.

[AS11]   Y. Adato and O. Shahar. "Specular Flow and Shape in One Shot". In: *BMVC 2011 - Proceedings of the British Machine Vision Conference 2011* (Jan. 2011). doi: 10.5244/C.25.24.

[Li14]   H. Li, T. Song, Z. Wu, J. Ma, and G. Ding. "Shape from Specular Flow with Near-Field Environment Motion Field". In: *Bebis G. et ak. (eds) Advances in Visual Computing* vol 8887 (2014). Lecture Notes in Computer Science. doi: https://doi.org/10.1007/978-3-319-14249-4_35.

Appendices

A.1 Further illustrations of the VSHOT system

Figure A.1 illustrates the complex measurement set-up of the VSHOT system in-field. The target distance towards the concentrator is about two times the focal length of the concentrator. The laser is calibrated with the optical rail which is carried out by the operator. In figure A.2 the camera calibration is illustrated. The camera is placed far away from the target on the camera arm extension. The pattern on the target is used to calibrate the camera.
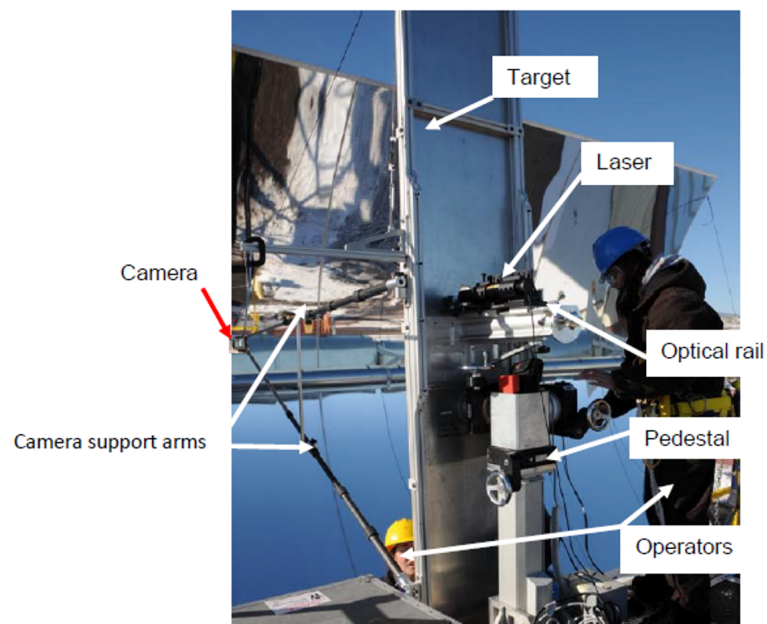
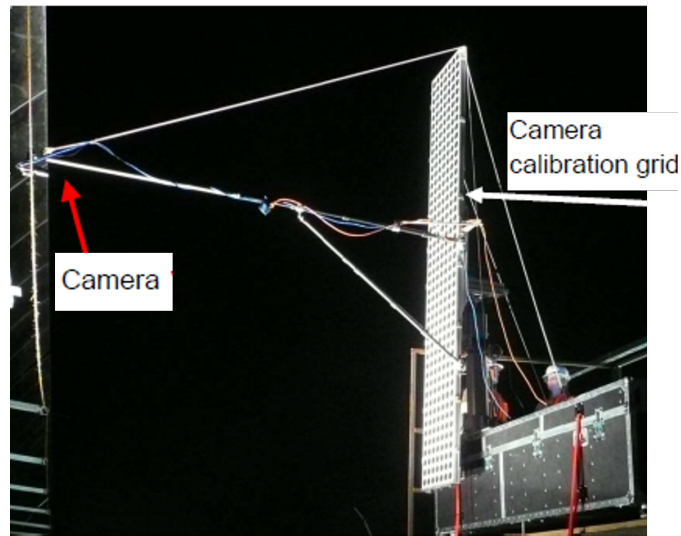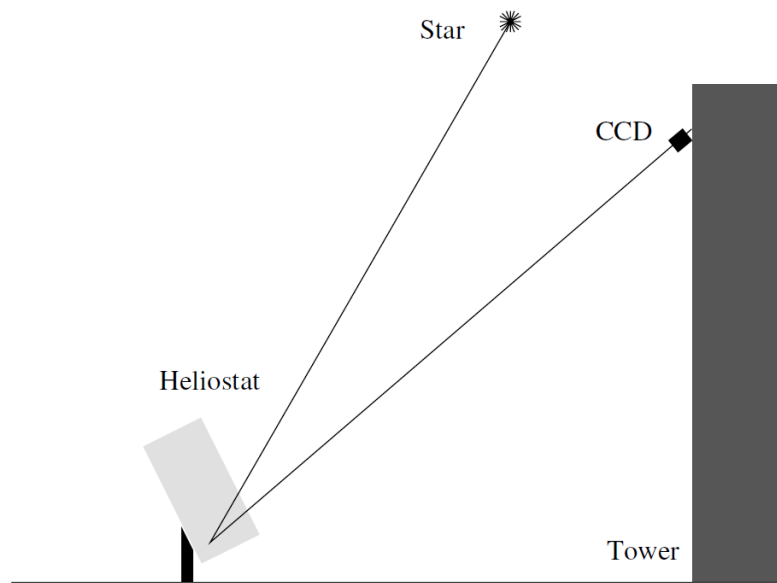**Figure A.1:** VSHOT: Measurement set-up (Image from [GLW10])

Figure A.2: VSHOT: Camera calibration (Image from [GLW10])

A.2 SCCAN measurement set-up

Figure A.3 illustrates the set-up of the SCCAN measurement system. During one total measurement the camera and the heliostat stay in position. The spatial position of the star relative to the ground system changes during time and allows to characterize the entire surface of a heliostat. One image of a measurement cycle is illustrated in figure A.4. The lit contour in the image is the reflection of one star towards the camera. The bright lines are distributed over the entire heliostat. Reason for this is the far-field illumination identical to the reflection of sun rays and the camera's position out of the heliostats focus point.

Figure A.3: SCCAN: Measurement set-up (Image from [AJV03])
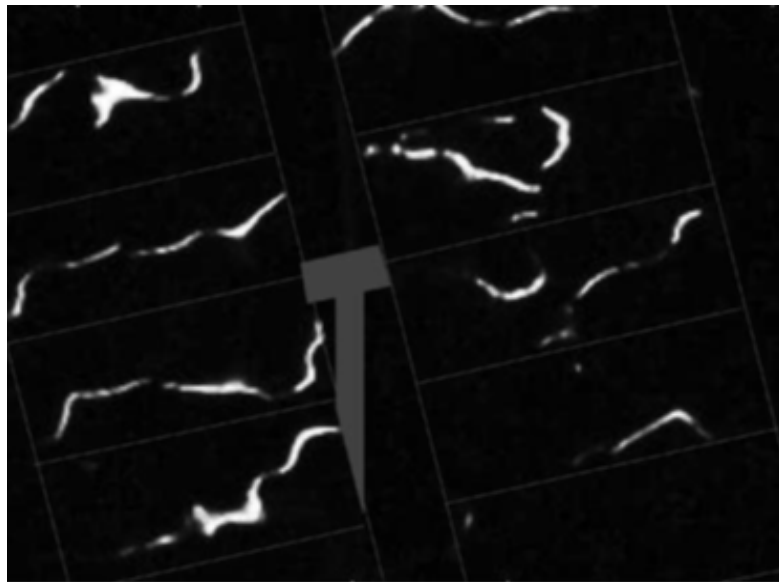
Figure A.4: SCCAN: Captured image (Image from [AJV03])